INFRARED IMAGING METHOD FOR THERMOGRAPHIC CHARACTERIZING OF MEDICAL HIGH INTENSITY FOCUSED ULTRASOUND DEVICES

By

MOHAMMADREZA JAHANGIR MOGHADAM

Presented to the Faculty of the Graduate School of
The University of Texas at Arlington in Partial Fulfillment
for the Degree of

MASTER OF SCIENCE IN ELECTRICAL ENGINEERING

THE UNIVERSITY OF TEXAS AT ARLINGTON
MAY 2012

ACKNOWLEDGEMENTS

I am sincerely thankful to my advisor, Professor Kambiz Alavi for his continued support and contribution in the development of my research. His clear vision and expert guidance has helped me stay on track and made successful completion of my work possible. I would also like to express my gratitude to my thesis committee members: Dr. Jonathan Bredow, Dr. Wendell Allan Davis, and Dr. Baohong Yuan. I would like to acknowledge Dr. Jashua Soneson from US Food and Drug Administration (FDA) for his guidance and providing HIFU simulator v1.2 .

I would like to thank Dr. Baohong Yuan for his support and making available his high frequency ultrasound set up for the experiments. I would like to acknowledge the Department of Biomedical Engineering and Dr. Baohong Yuan's research team members Jayanth Kandukuri , Peter Leboulluec and Yuan Liu for their help and support.

I would like to thank my parents Homa and Alireza, my brother Milad and my sister Mahkam for their constant encouragement and support without which this work would have not been possible. I would like to thanks to all my UT Arlington friends and my family Mahboobeh, Mahnaz, Ross, Shahriar, Neema, Mauny, Ali and Aria.

Finally, but really foremost, I thank the Lord, for the strength, intelligence, perseverance and wisdom he has given me to realize my dreams and perform this work.

April 18, 2012

ABSTRACT

HI SPEED INFRA-RED IMAGING METHOD FOR TEMPORAL CHARACTERIZING OF MEDICAL HIGH INTENSITY FOCUSED ULTRASOUND DEVICES

Mohammadreza Jahangir Moghadam, M.S
The University of Texas at Arlington, 2012

Supervising Professor: Professor Kambiz Alavi.

With new improvements in high-end commercial R&D Infrared camera technologies many challenges have been overcome for exploring high speed Infrared imaging, the ability to capture fast varying phenomena without image blur, acquire enough data to properly characterize dynamic energy, and increase the dynamic range without compromising the number of frames per second. This study presents a noninvasive method for determining the spatial and thermal heating profiles in a phantom tissue generated by High Intensity Focused Ultrasound (HIFU) beam by using Infrared imaging. A high speed Infrared camera was placed above a tissue mimicking material that was heated at the focal point of HIFU with no other sensors present in the HIFU axial beam. This setup eliminates interference caused by parasitic objects present in the field. A silicone tissue phantom was used and sonicated with a 2.5 MHz HIFU transducer at pulse cycle of 200ms and burst time of 20ms. The temperature rise over the surface of the phantom was measured using an Infrared camera. A MATLAB simulation code used to perform a finite-element solution to the pressure wave propagation and heat equations inside the phantom and temperature rise to the phantom was computed. Three different power levels of HIFU transducers were used in measurement and simulation predicted temperature increase values were within about 25% of IR measurements. The temperature measurements taken may also be used to detect the axial focal point of the HIFU with accuracy of 10%.

TABLE OF CONTENTS

APPENDIX

LIST OF ILLUSTRATIONS

Figure Page

LIST OF TABLES

Table Page

CHAPTER 1

INTRODUCTION

1.1 Background and significance of HIFU

The discovery of piezoelectricity by the Curies in 1880 using natural quartz was the beginning of using ultrasound as an energy source for many ultrasonic applications, however the applications of ultrasound in medicine did not begin until shortly after the 2nd World War. The main applications of ultrasound during this time were to develop SONAR for underwater navigation, communication and to detect other vessels. The publication by Dr. Karl Theodore Dussik in Austria in 1942 on their work on transmission ultrasound investigation of the brain was the first published medical ultrasonic application [ref 1].

Ultrasound is a form of energy consisting of mechanically produced waves of frequencies above the range of human hearing. The frequency of these waves typically ranges from 20 kHz to several hundred MHz. Ultrasound is commonly thought of as a diagnostic imaging modality, but therapeutic applications involving High Intensity Focused Ultrasound (HIFU) are rapidly emerging.

HIFU is produced by concave transducers or plane disk transducers with acoustic lenses that focus the ultrasound beam on a focal region as small as few millimeters. This intense energy deposition at the focus can rapidly increase the temperature in a very short time causing immediate cell necrosis in the targeted region. Most commercially available HIFU devices work in a frequency ranges of 1 to 5 MHz.

In the past two decades, HIFU has been receiving more attention by different research groups and companies as a non-invasive procedure to treat cancers in different organs, such as kidney [2]-[4], liver [5], brain [6], prostate [7], and breast [8].

HIFU is currently classified as a Class III device, which is subject to pre-market approval (PMA), by the United States Food and Drug Administration (FDA). Class III devices are those that support or sustain human life, are of substantial importance in preventing impairment of human health, or which present a potential, unreasonable risk of illness or injury.

PMA approval is based on a determination of the FDA that the PMA contains sufficient valid scientific evidence to assure the device is safe and effective for its intended use. Ongoing standard establishment process competition has turned HIFU research into a very interesting topic for scientists in this field. For example the clinical trial studies on Sonablate®500 devices for the treatment of prostate cancer with HIFU is being performed at only 14 FDA approved locations in United States as of November 2011 [9].

Table 1.1 Trial centers for treatment of prostate cancer with HIFU

Medical Center / Research center		Location
1	David Geffen School of Medicine	University of California Los Angeles
2	VA Connecticut Healthcare System	Yale University
3	Walter Reed Army Medical Center	Washington, District of Columbia
4	Specialists in Urology	Naples, Florida
5	Indiana University	Indianapolis, Indiana
6	Tulane University	New Orleans, Louisiana
7	Montefiore Medical Center	Bronx, New York
8	University of Cincinnati	Cincinnati, Ohio
9	Urologic Consultants of SE PA, LLP	Bala Cynwyd, Pennsylvania
10	University of Wisconsin Comprehensive Cancer Center	Madison, Wisconsin
11	Urology Associates of North Texas	Arlington, Texas
12	University of Texas M.D. Anderson Cancer Center	Houston, Texas
13	Florida Urology Specialists	Sarasota, Florida
14	Metropolitan Urology, PSC	Jeffersonville, Indiana

1.1.1. HIFU Standards

International Electro technical commission (IEC) standards such IEC-62649(2010) and IEC-61157 (2007) specifies a standard means and format for the reporting of the acoustic output of medical diagnostic ultrasonic equipment. The numerical values for reporting purposes represent the average values for the maximum output conditions for a given operating mode and are derived from measurements made in water. Intensity parameters are specified in these standards, but mostly regarded as derived quantities that are meaningful only under certain assumptions related to the ultrasonic field being measured. This International standard is applicable to medical diagnostic Ultrasonic equipment like HIFU. It provides a set of traceable acoustic parameters describing the acoustic fields and defines a standard means and format for the reporting of the acoustic output information. It also describes a reduced dataset recommended for equipment generating low acoustic output levels.

The principal problem with the measurement of HIFU fields is that the Ultrasound field is of sufficient intensity that it can destroy or significantly alter the properties of the measurement device. The measurement device must have the capability of repeatedly measuring ultrasound fields over a wide frequency range with relatively flat frequency response (from 500 KHz to 20 MHz, when harmonics are included), with small apertures (less than 0.5mm), at high intensities (over 50 W/cm^2) [10].

The general requirements for sensors to be used in high energy ultrasound fields were presented and studied by Schafer and Lewin [11]. Spatial and temporal distribution of acoustic parameters can be obtained using hydrophones. The bandwidth and linearity requirements would generally be met using a piezopolymer material, such as polyvinylidene difluoride (PVdF). This material, however, is relatively fragile, and would literally melt or would otherwise be damaged if directly exposed to the intensity levels produced by HIFU devices. One approach uses a disposable piezopolymer film, which is designed to be self-monitoring. This approach solves the problem of bandwidth and linearity, and it addresses the issue of changes in the sensitivity in the material caused by exposure to the high intensity ultrasound.

High intensities of force and heat generated by focused ultrasound generates cavitation or bubbling. Dissolved gases are drawn out of a solution producing bubbles, when the acoustic pressure falls below the vapor pressure of the medium [12].

The micro-bubbles can shield the sensor from the HIFU beam, thereby preventing accurate measurement of acoustic parameters. Micro-bubbles can also be used as an imaging enhanced method in the MRI guided focused Ultrasound method [13].

With development in high energy ultrasound investigation micro-bubbles and cavitation are playing an increasingly significant role in both diagnostic and therapeutic applications of ultrasound. Micro-bubble ultrasound contrast agents have been in clinical use now for more than two decades [14], stimulating the development of a range of new contrast-specific imaging, and techniques which offer substantial benefits in echocardiography, microcirculatory imaging, quantitative and molecular imaging. In drug delivery and gene therapy, micro-bubbles are being investigated as vehicles which can be loaded with the required therapeutic chemical agent, traced to the target site using diagnostic ultrasound, and then destroyed with ultrasound of higher intensity energy burst to release the material locally. This method reduces side effects associated with systemic administration or toxic chemotherapy.

1.1.2. Noninvasive methods of measurement

In the regulatory review of HIFU systems, the first step is the characterization of the device in a liquid and tissue-mimicking medium. This procedure involves the determination of the total acoustic power and the spatial intensity distribution within the medium. The second step is the measurement of temperature rise within a tissue mimicking material. Due to the destructive potential of HIFU, characterization of the beam at clinically relevant powers can be difficult to perform using standard techniques. It is therefore worthwhile to pursue noninvasive methods to measure intensity and temperature within the tissue-mimicking material. The configuration for such an experiment includes pulse generator or power amplifier, tissue mimicking material, receiver or detector, and data acquisition system. The standard medium for applying experiments is degassed and deionized (DI) water to reduce the effects of dissolved chemicals and gasses. Figure 1.1 shows the basic configuration for HIFU measurements.

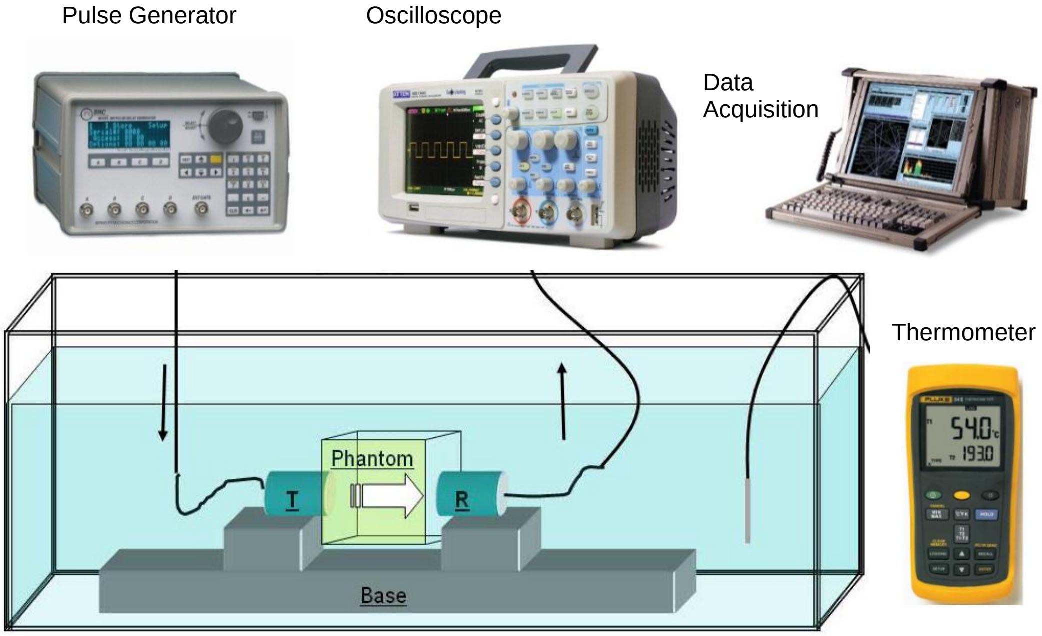

Figure 1.1 Standard HIFU and TMM test configuration

Several techniques are currently used for non-invasive HIFU power measurements. For medical work, the characterization of acoustic output is often performed in two parts. First, measurements are performed in water. Next, a method is used to relate the measurements in water to what is expected in tissue [15]. Although this approach is widely used in medical applications, the challenge of directly measuring and modeling HIFU fields is ongoing.

Experimental tools and numerical models are improving over time, but no standard method has yet been agreed upon for HIFU device.

The most common parameter to characterize the acoustic output of a HIFU device is the spatially averaged intensity (I_{SAL}). The calculation of I_{SAL} for a given source is achieved through measurement of the acoustic power output of the device and the focal cross-sectional area of the HIFU beam which is a plane parallel to the surface of the device with maximum heat intensity. The acoustic power output is measured using a radiation force balance. The focal cross-sectional area is determined by scanning a hydrophone across the focal plane of the source. The spatially averaged intensity is then calculated by dividing the acoustic power that passes within the −6 dB pressure contour by the area of the contour. Acoustic propagation is assumed to be linear in that the frequency content of the pressure waveform and the corresponding heating area width is assumed to be independent of the source power. The peak positive and peak negative pressures for sinusoidal waveforms are therefore equal and only one need to be measured. The low-power measurements of I_{SAL} are then linearly extrapolated to higher output levels of the HIFU device. That is, the focal pressure amplitude is assumed to scale linearly with applied source voltage so that the focal intensity increases as a square of the voltage.

Once the output intensity is determined in water, it can be used to estimate the focal intensity in tissue. This step is achieved calculating the heat intensity depending on the propagation path and attenuation coefficient of tissue at the operating frequency of the source. This approach is useful for comparing exposures at relatively low intensities as it provides an estimate of the *in situ* focal intensity. Tissue heating can also be estimated from the product of the tissue absorption coefficient and I_{SAL}. However, the acoustic medium of most HIFU clinical devices are nonlinear; therefore, errors are introduced at every characterization step where linear acoustic propagation is assumed.

The characterization of medical acoustic devices that operate at high output levels has been a research topic and an issue of practical concern for several decades [17] . The importance of nonlinear effects has been considered and addressed at diagnostic levels. These effects are critical as acoustic pressures of up to 100 MPa or higher can be reached.

Direct measurements of pressure waveforms in HIFU fields require a hydrophone that is robust to mechanical damage from cavitation and that has a large bandwidth to capture sharp shock fronts that can develop at the focus. Waveform measurements in HIFU are very difficult because of the explicit need to accurately measure peak amplitudes of shock waves within a relatively small focal region. Accurate measurement of peak pressures is especially relevant in HIFU because the prediction of heating rates is sensitive to shock amplitudes. When shocks are present, the amount of heat deposition is determined by the cube of the shock amplitude [18] .This imposes additional requirements on hydrophone bandwidth. New commercially available HIFUs use higher frequencies to achieve stronger shockwaves. The typical size of the HIFU focal zone becomes smaller in both transverse and axial directions as the frequency increases. Table 1.2 shows different focal volume size vs. frequency for Sonic concept® company HIFUs

Table 1.2 Effect of frequency increase on focal volume size

Model	Frequency(MHz)	Power (Watt)	Focal Volume Size (mm)
H-101	1.1	400	1.26 X 11.0
H-106	2	400	0.73 X 7.0
H-108	2.5	400	0.5 x 3.5
SU-108	5	400	0.32 X 3.0

As mentioned, direct measurements of high amplitude fields are mostly performed in water, and methods have been described to measure nonlinear field transducers. Recently, shocked waveforms from a HIFU source were measured using a fiber optic probe hydrophone (FOPH) [19] . Such hydrophones claim advantages of self-calibration, small size, and broad bandwidth relative to described polyvinylidene fluoride (PVDF) hydrophones [21].

1.1.3. Numerical nonlinear modeling methods for HIFU devices

Numerical modeling has been used to predict high amplitude acoustic fields from medical devices. One advantage of modeling is that it can be used to determine the acoustic field in both water and tissue, because inserting hydrophones or thermocouples inside the tissue mimicking device can alter the high intensity ultrasound waves. Changing the location and depth of a receiver is also impossible in the viscous tissue mimicking material.

Numerical algorithms, most commonly based on the nonlinear parabolic Khokhlov–Zabolotskaya–Kuznetsov (KZK) as shown in Equation 1.1

$$\frac{\partial}{\partial \tau}\left[\frac{\partial p}{\partial z} - \frac{\beta}{\rho_0 c_0^3} p \frac{\partial p}{\partial \tau} - L_{abs}(p)\right] = \frac{c_0}{2} \nabla_{\perp}^2 p \tag{1-1}$$

where p is the acoustic pressure, z is the propagation coordinate along the axis of the beam, $\tau = t - z/c_0$ is the retarded time, c_0 is the ambient sound speed, ρ_0 is the ambient density of the medium, β is the coefficient of nonlinearity, $\nabla_{\perp}^2$ is the Laplacian with respect to the transverse coordinate r, and L_{abs} is the linear operator that accounts for the absorption and dispersion of the medium [21].

Considering the nonlinear equation in modeling is important for higher intensity powers. When a sound wave propagates through a material as a localized pressure shockwave, increasing the pressure of a material increases its temperature and the speed of sound in compressible material increases with temperature; as a result, the wave travels faster during the high pressure phase of the oscillation than during the lower pressure phase. This affects the wave's frequency structure. For example, in a plane sinusoidal wave at a single frequency, the peaks of the wave travel faster than the troughs, and the signal becomes more like a saw tooth wave as shown in Figure 1.2.

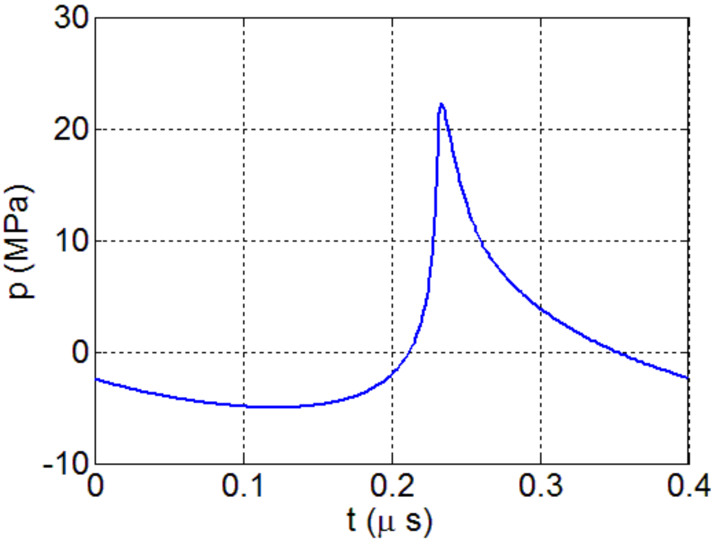

Figure 1.2 Nonlinear distortion of 2.5 MHz sinusoidal pressure wave vs. time

1.1.4. Infrared imaging tool for HIFU devices

Finding an optimum simulation method and measurement technique that confirms the simulated result is still under investigation. Infrared (IR) thermography is a potentially useful method for inferring this field intensity from the heating pattern within the phantom or tissue mimicking material (TMM). Infrared imaging is a non-contact and non-invasive method. However, IR measurements require an air layer between the phantom and the camera, making inferences about the thermal field in the absence of the air complicated. For example, convection currents can arise in the air layer and distort the measurements relative to the phantom-only situation. Although this method has its own short comes, it is preferred over using an array of thermocouples inside the material to investigate temperature patterns.

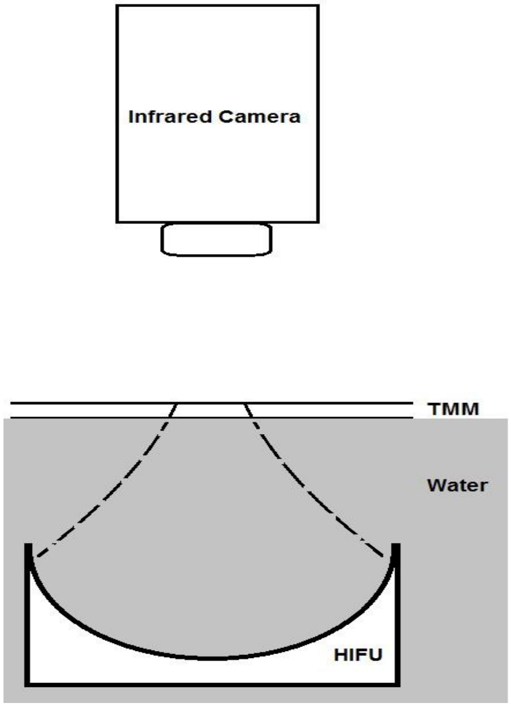

Figure 1.3 HIFU Infrared measurement configuration

Quantitative predictions of intensity fields based upon IR temperature data are also complicated by axial and radial diffusion of heat. Simulating the temperature increase resulted from acoustic wave propagation is being performed by solving the Bio Heat Transfer (BHT) equation [22]. Bio heat transport equations can be applied to the process of energy deposition into the tissue as well as the subsequent conduction or convection heat transport to cells neighboring the targeted site to predict a temperature history and distribution.

The three-dimensional expression of Pennes' bio heat equation in an isotropic uniform media with uniform material properties is given by Equation 1.2

$$\rho C \frac{\partial T}{t} = \mathrm{k}\nabla^2 T + H - wCT \tag{1.2}$$

where T is temperature in℃ , ρ is tissue density, C is specific heat, H is heating rate from the source, and w is perfusion rate. Commercially available software like PZFlex, from Weidlinger Associates Inc., CA uses a finite-element solution to the wave propagation and Bio Heat Transfer (BHT) equations within the phantom.

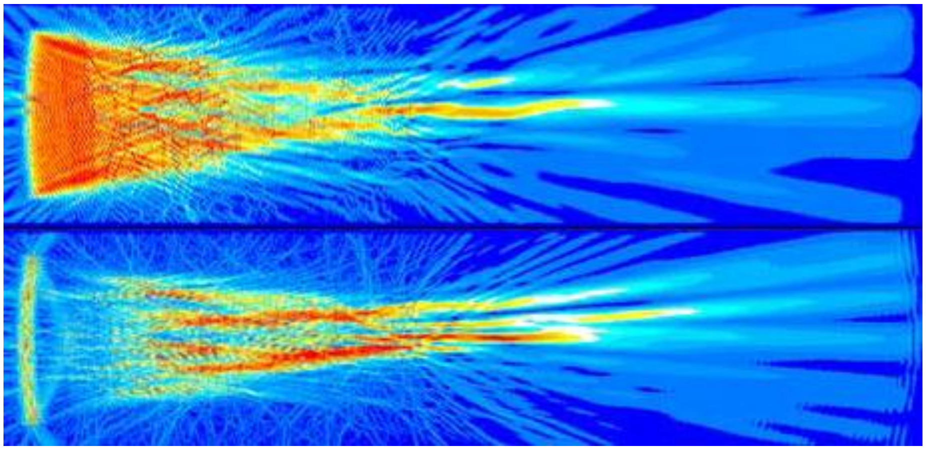

Figure 1.4 Pressure distribution in tissue at fundamental and second harmonic frequency (Courtesy PZflex)

1.1.5. Modeling method requirements for HIFU devices

The submission of preclinical (i.e., bench, *in vitro*, or *in vivo* on animal) testing is a necessary part of the process to establish that the device is capable of operating in a safe and effective manner. Unlike other medical applications of ultrasound such as physiotherapy, diagnostic imaging, and extracorporeal shock wave lithotripsy, there are no recognized consensus standards or guidance documents for HIFU. Thus, standardized methods currently are unavailable for measuring the acoustic output and beam/focusing characteristics, and for relating these measurements to the distribution of temperature in tissue. To obtain this information in the absence of well characterized standard techniques, the FDA's regulatory evaluations of the pre-clinical testing results are performed on a case-by-case basis [16]. However, the pre-clinical testing data submitted by device sponsors should usually include the following elements:

- Verification of the basic system/transducer design and performance by measuring free field ultrasonic power output and focusing characteristics.
- Demonstration that the device can produce predictable thermal lesions via both measurements of temperature distributions *in vitro* and computational modeling.
- Demonstration of the safety of non-targeted tissues both proximal and distal to the targeted region through acoustic and thermal measurements and computational modeling.
- Demonstration of the accuracy of the method for targeting the region of interest and for monitoring the progress or result of treatment, if applicable.

This thesis describes a noninvasive technique that involves infrared imaging of a material that has been heated by absorbed HIFU energy. This measurement method and simulation result obtained by numerical solutions of the BHT and KZK differential equations can help achie new methods and standards for the above requirements. The most important part of the measurements in this research are from the Infrared camera with advanced non uniformity and emissivity correction for thermal video processing. The main concept of these corrections comes from principal of blackbody radiation and emissivity.

1.2 Infrared radiation and detection

All bodies with temperature above absolute zero emit photons. This phenomenon is known as thermal radiation. For bodies with temperature near 300 K the predominant portion of the radiation is not visible to the human eye. However, it can be sensed as heat. As the temperature of a body is increased, more radiation is emitted, and the dominant portion of its spectrum shifts so that its radiation begins to be visible to humans. Thermal radiation is called infrared radiation (IR), and it covers the [0.77 μm – 1000 μm] range of the electromagnetic spectrum as shown in Figure1.5.

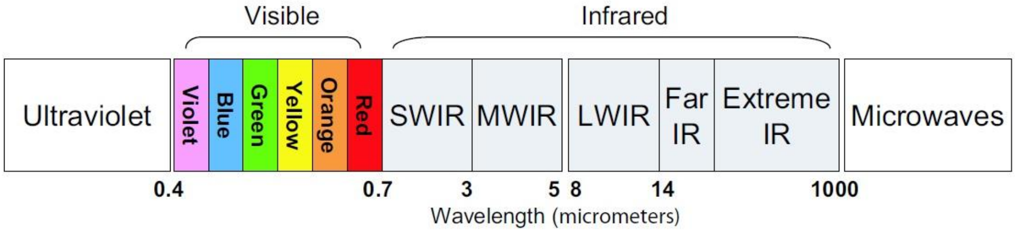

Figure 1.5 Infrared bands and their position in the electromagnetic spectrum

The infrared band is often further subdivided into four smaller bands, the boundaries of which are also arbitrarily chosen. They include: the near infrared (0.75–3 μm), the middle infrared (3–6 μm), the far infrared (6–15 μm), and the extreme infrared (15–100 μm).

1.2.1. Black-body radiation

A blackbody is defined as an object which absorbs all radiation that impinges on it at any wavelength. The apparent misnomer, black, relating to an object emitting radiation is explained by Kirchhoff's Law (after Gustav Robert Kirchhoff, 1824–1887), which states that a body capable of absorbing all radiation at any wavelength is equally capable in the emission of radiation. The construction of a blackbody source is, in principle, very simple. The radiation characteristics of an aperture in an isotherm cavity made of an opaque absorbing material represents almost exactly the properties of a blackbody. A practical application of the principle to the construction of a perfect absorber of radiation consists of a box that is light tight except for an aperture in one of the sides. Any radiation which then enters the hole is scattered and absorbed by repeated reflections so only an infinitesimal fraction can possibly escape. The blackness which is obtained at the aperture is nearly equal to a blackbody and almost perfect for all wavelengths.

By providing such an isothermal cavity with a suitable heater it becomes what is termed a cavity radiator. An isothermal cavity heated to a uniform temperature generates blackbody radiation, the characteristics of which are determined solely by the temperature of the cavity. Such cavity radiators are commonly used as sources of radiation in temperature reference standards in the laboratory for calibrating thermo graphic instruments.

If the temperature of blackbody radiation increases to more than 525 °C (977 °F), the source begins to be visible so that it appears to the eye no longer black. This is the incipient red heat temperature of the radiator, which then becomes orange or yellow as the temperature increases further. In fact, the definition of the so-called color temperature of an object is the temperature to which a blackbody would have to be heated to have the same appearance. Three expressions that describe the radiation emitted from a blackbody are Planck’s law, Wien’s displacement law and Stefan-Boltzmann's law.

1.2.1.1 Planck’s law

Max Planck (1858–1947) was able to describe the spectral distribution of the radiation from a blackbody by means of the equation (1.3)

$$W_{\lambda b} = \frac{2\pi hc^3}{\lambda^5 (e^{hc/\lambda KT} - 1)} 10^{-6} [Watt/m^2 \mu m] \tag{1.3}$$

$W_{\lambda b}$ is blackbody spectral radiant emittance at wavelength λ, c is the velocity of light, h is Planck's constant, k is Boltzmann's constant, T is absolute temperature of the blackbody in Kelvin and λ is wavelength.

Planck's formula, when plotted graphically for various temperatures, produces a family of curves as shown in Figure 1.6 . Following any particular Planck curve, the spectral emittance is zero at λ = 0, then increases rapidly to a maximum at a wavelength λ_{max} and after passing it approaches zero again at very long wavelengths. The wavelength at which maximum occurs becomes shorter as the temperature increases.

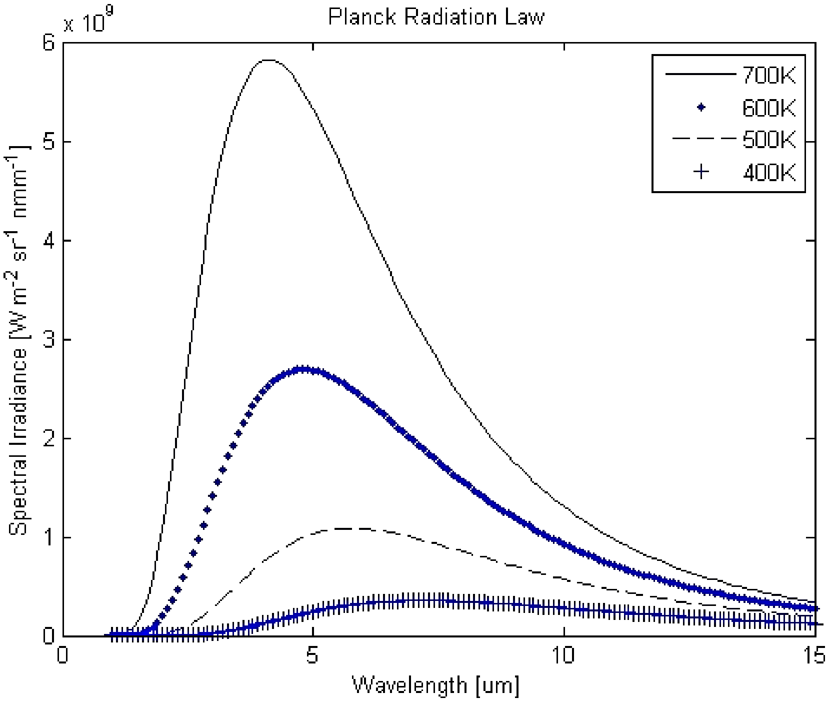

Figure 1.6 Blackbody spectral radiant emittance according to Planck's law for 400-700K

1.2.1.2 Wien's displacement law

By differentiating Planck's formula with respect to λ, and finding the maximum, we have Wien's formula (after Wilhelm Wien, 1864–1928), which expresses mathematically the common observation that colors vary from red to orange or yellow as the temperature of a thermal radiator increases.

$$\lambda_{max} = \frac{2898}{T}\,(\mu m) \tag{1.4}$$

The wavelength of the color is the same as the wavelength calculated for λ_{max}. A good approximation of the value of λ_{max} for a given blackbody temperature is 3000/T (μm). Thus, a very hot star such as Sirius (11,000 K), emitting bluish-white light, radiates with the peak of spectral radiant emittance occurring within the invisible ultraviolet spectrum, at a wavelength of 0.27 μm. The sun (approx. 6 000 K) emits yellow light, peaking at about 0.5 μm in the middle of the visible light spectrum.

At room temperature (300 K) the peak of radiant emittance lies at 9.7 μm, in the far infrared, while at the temperature of liquid nitrogen (77 K) the maximum of the almost insignificant amount of radiant emittance occurs at 38 μm, in the extreme infrared wavelengths.

1.2.1.3 Stefan-Boltzmann's law

By integrating Planck's formula from λ = 0 to λ = ∞, total radiant emittance (W_b) of a blackbody can be obtained as

$$W_b = \sigma\, T^4 \tag{1.5}$$

Equation (1-5) is the Stefan-Boltzmann formula (after Josef Stefan, 1835–1893, and Ludwig Boltzmann, 1844–1906), which states that the total emissive power of a blackbody is proportional to the fourth power of its absolute temperature. Graphically, W_b represents the area below the Planck curve for a particular temperature. It can be shown that the radiant emittance in the interval λ = 0 to λ_{max} is only 25 % of the total, which represents about the amount of the sun's radiation which lies inside the visible light spectrum. Stefan-Boltzmann formula can be used to calculate the power radiated by the human body, at a temperature of 300 K and an external surface area of 2 m^2 with a result of around 1 kW. This power loss could not be sustained if it were not for the compensating absorption of radiation from surrounding surfaces.

1.2.2. Non-Blackbody radiators

Real objects almost never comply with mentioned laws over an extended wavelength region, although they may approach the blackbody behavior in certain spectral intervals. A fraction of the incident radiation may be absorbed, reflected, or transmitted. All of these factors are more or less wavelength dependent.

Emissivity describes the fraction of the radiant emittance of a blackbody produced by an object at a specific temperature. The spectral emissivity is defined as the ratio of the spectral radiant power from an object to that from a blackbody at the same temperature and wavelength.

$$\varepsilon_\lambda = \frac{W_{\lambda 0}}{W_{\lambda b}} \tag{1.6}$$

With respect to Equation 1.6 , there are three types of radiation source distinguished by the ways in which the spectral emittance of each varies with wavelength:

- Blackbody, for which ε_λ= ε = 1.
- Gray body, for which ε_λ= ε = is less than 1.
- Selective radiator, for which ε varies with wavelength.

For a gray body radiator, the Stefan-Boltzmann formula becomes:

$$W = \varepsilon\sigma T^4 \tag{1.7}$$

This states that the total emissive power of a gray body is the same as a blackbody at the same temperature reduced in proportion to the value of ε from the gray body. Figure 1.7 shows the comparison of the spectral exitance from a blackbody, graybody with ε = 0.6, and a selective radiator. The blackbody exitance curve is the ideal maximum for all wavelengths.

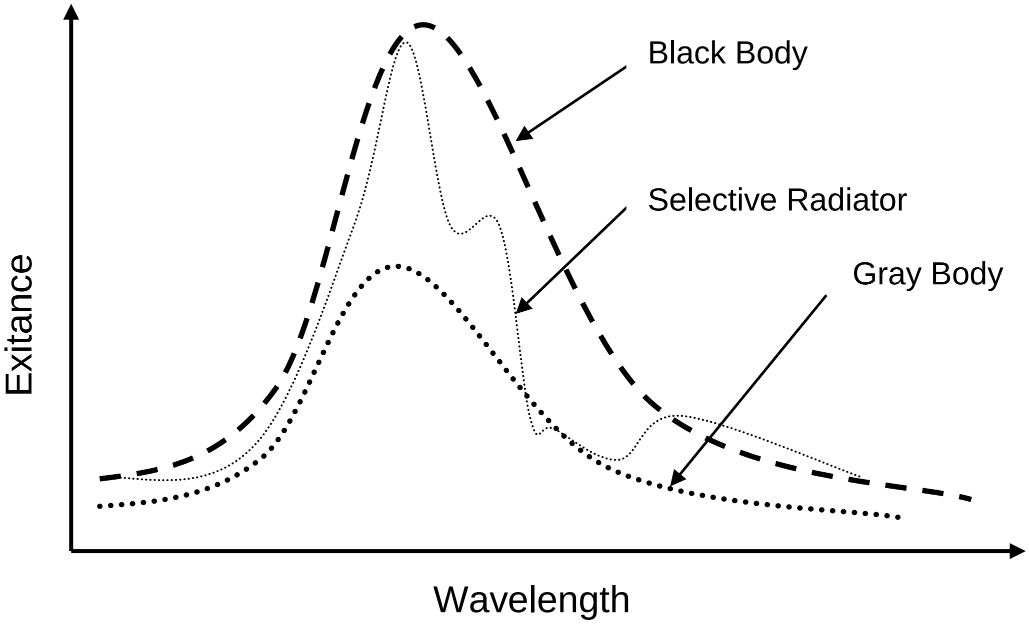

Figure 1.7 comparison of the spectral exitance for black, gray and selective body

1.2.3. Radiometric measurements with Infrared camera

There are five basic steps in producing radiometric and thermo graphic measurements with an IR camera system:

1. The target object has a certain energy signature that is collected by the IR camera through its lens.

2. This involves the collection of photons in the case of a photon detector.

3. The collected energy causes the detector to produce a signal voltage that results in a digital count through the system's A/D converter. (For example, the FLIR ThermoVision® SC6000 IR camera has a 14-bit dynamic range in its A/D converter, which creates count values ranging from 0–16,383.

4. When the camera is calibrated, digital counts are transformed into radiance values.

5. The calibrated camera‘s electronics convert radiance values to temperature using the known or measured emissivity of the target object.

Expanding on Steps 4 and 5, an effective blackbody temperature measurement can be derived from a radiance measurement by applying a radiometric calibration, temperature vs. radiance model, and emissivity of the target object or scene. Every IR camera designed for serious measurements is calibrated at the factory. In the calibration lab, the camera takes a number of blackbody measurements at known temperatures, radiance levels, emissivities, and distances. This creates a table of values based on the A/D counts from the temperature/radiance measurements.

Once the counts for each blackbody temperature measurement are entered into the calibration software, the data are then passed through an in-band radiance curve fit algorithm to produce the appropriate in-band radiance vs. count values given the camera system's normalized spectral response function. This produces a radiometric calibration of in-band radiance [W/(sr-cm2)] versus the digital counts obtained while viewing a blackbody over a range of temperatures. The result is a series of calibration curves. The calibration curves are stored in the camera system’s memory as a series of numeric curve fit tables that relate radiance values to blackbody temperatures. When the system makes a measurement, it takes the digital value of the signal at a given moment, goes into the appropriate calibration table, and calculates temperature. Due consideration is given to other factors like atmospheric attenuation, reflected ambient temperature, and the camera’s ambient temperature drift before the final result is presented.

1.2.4. Infrared detector for camera standards

Several standards have been developed for Infrared cameras beside ISC-9705. One of the most important companies that have developed such standards for Infrared cameras is Indigo Systems Corporation, (Santa Barbara, CA). Indigo Systems is a leading developer and manufacturer of infrared cameras for commercial, industrial, scientific, R&D, military, and OEM applications. Indigo Systems Corporation has developed a family of Standard Readout Integrated Circuits (ROIC) for use in infrared focal plane array (FPA) imaging systems. These standard ROIC’s are designed to provide a complete set of operating features for camera level FPA control, while also providing high performance capability with any of several detector materials. By creating a uniform electrical interface for FPA’s, these standard ROIC’s simplify the task of FPA integration with imaging electronics and physical packages. The block diagrams, specifications, and technical terms used for Infrared camera in this thesis are based on Indigo system standards. Measurements of this thesis were possible by using specific features of FLIR SC6000 camera. For this reason some features of such cameras are briefly discussed in the next chapter.

1.3 Features of Infrared cameras with Indigo's standard ROIC

Indigo's standard Readout Integrated Circuit (ROIC) include a detector, digitizer, a Non Uniformity Correction (NUC) stage, a Bad pixel replacement (BPR) , data output stages, video generation , frame rate control, integration control, and a camera control as shown in Figure 1.8.

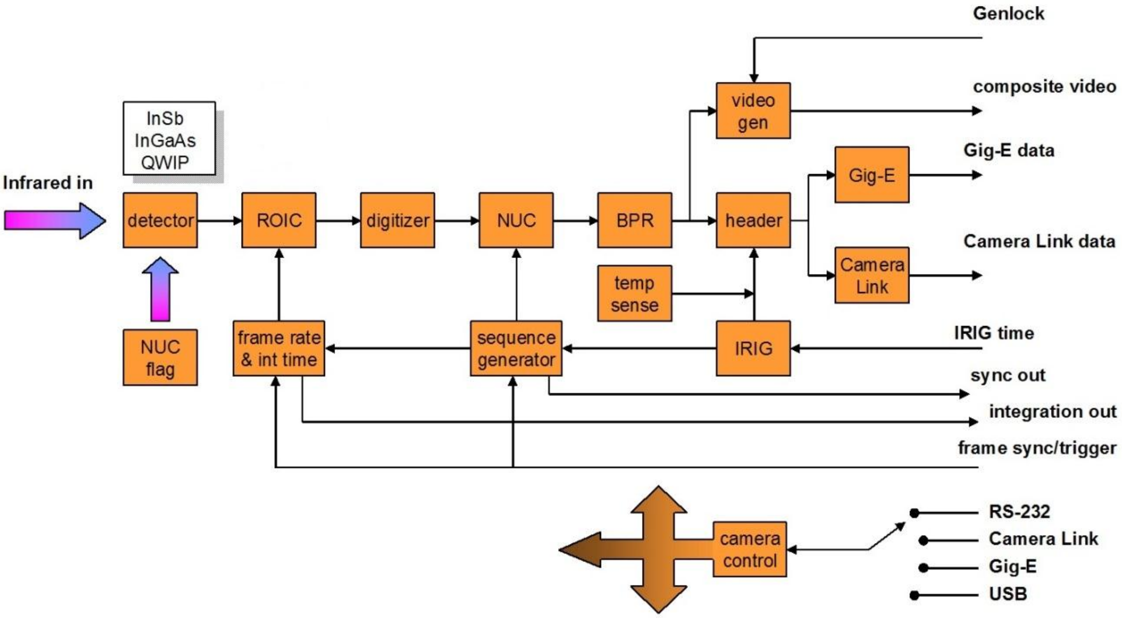

Figure 1.8 Features inherent in Indigo's standard ROICs, Courtesy FLIR

1.3.1. Infrared camera detectors

Several technologies and materials are available for design of Infrared detector. This is the key part an Infrared camera. Mercury Cadmium Telluride (MCT), InSb InAsSb, GaAs or AlGaAs Quantum Well Infrared Photo detectors (QWIP) are materials that are currently being

used to build Focal Plane Arrays (FPA). These materials have different band gaps, sensitivity, detection bandwidth and working temperatures. The sensor assembly is generally an all-metal evacuated dewar assembly cooled by a closed-cycle Stirling cryogenic cooler to a temperature of approximately 77° K.Figure 1.9 shows different Relative response curves for a number of IR cameras vs. wavelength. The InSb Infrared camera used in this research has a better flat response over the wavelength in comparison with GaAs and QWIP Infrared cameras.

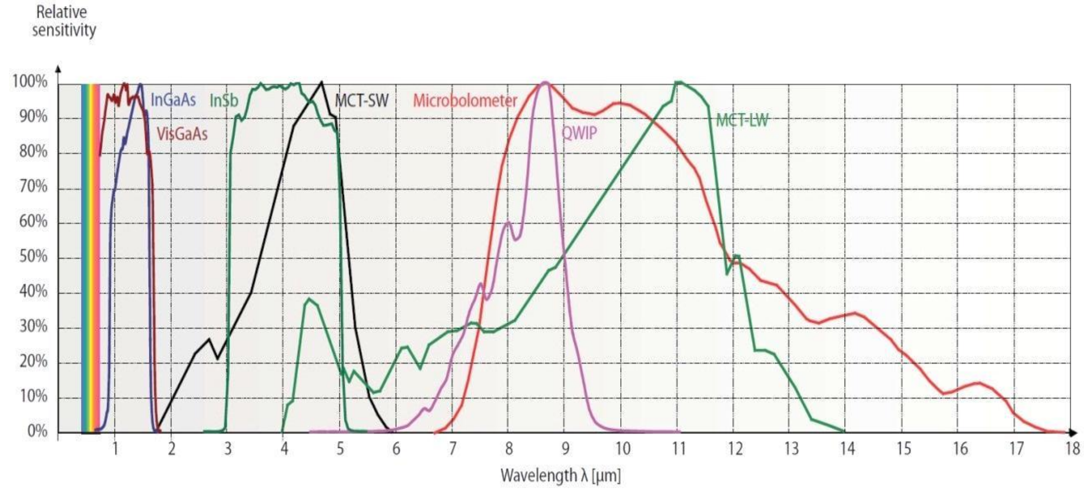

Figure 1.9 Relative response curves for a number of IR cameras

1.3.2. Infrared camera behavior with varying frame rate, integration time and window size

The frame rate is defined as the number of snapshots taken per second. The integration time is defined as the length of time that each snapshot actually views the scene. The window size is the number of pixels in each direction of the FPA. Most Infrared cameras use the standard mode of camera operation as the Asynchronous Integrate While Read (AIWR) mode. As the name implies, the camera is able to integrate scene signal while simultaneously reading out the previous frame. This mode allows for semi-independent control of the camera's frame rate and integration time. The frame rate may be controlled by the camera (free run) or may be externally synchronized to synchronize camera with external events.

Window size is usually determined based on user needs and the amount of data can be processed or transferred each second. The maximum integration times are in turn, controlled by the selected frame rate. Time required to readout all of the pixels limits the maximum frame rate (frame time is the inverse of frame rate). The maximum frame rate is dependent on the window size. For example in SC6000 camera for a full frame of 640 x 512 pixels, the frame rate is limited to 126 Hz. By decreasing the windows size and integration time for the temperature range, it is possible to achieve higher frame rates as shown in the equation (1.8) .

$$Frame\ rate = \frac{50{,}000{,}000}{(rows + 3)(columns + 128) + 8} \tag{1.8}$$

Table 1.3 shows some achievable frame rates achievable based on equation (1.8). The selection of a smaller window to have higher frame rates limits the maximum integration time available. The pixel intensity vs. temperature calibration might be required for integration times less than recommended.

Table 1.3 Frame rate vs. window pixels

Picture columns (pixel)	Picture rows (pixel)	Frame rate (Hz)
640	512	120
320	200	470
128	128	1490
64	64	3880

CHAPTER 2

PRESSURE AND HEAT DIFFERENTIAL EQUATIONS

2.1 Computational method for KZK differential equations

The nonlinear parabolic KZK wave equation describes the effects of diffraction, absorption, and nonlinearity. Its axisymmetric form in terms of pressure can be written in the form of Equation 2.1

$$\frac{\partial^2}{\partial z \partial \tau} p = \frac{c_0}{2} \nabla_\perp^2 p + \frac{\delta}{2c_0^3} \frac{\partial^3 p}{\partial \tau^3} + \frac{\beta}{2\rho_0 c_0^3} \frac{\partial^2 p^2}{\partial \tau^2} \tag{2.1}$$

where p is the acoustic pressure, z is the propagation coordinate along the axis of the beam, $\tau = t - z/c_0$is the retarded time, c_0 is the ambient sound speed, $\rho_0$is the ambient density of the medium, β is the coefficient of nonlinearity, δ is diffusivity parameter. This equation describes directional sound beams and is valid for ka $\gg 1$, where k is the wave number and a is characteristic width of the source. [23, 24]

Sound diffusivity and the coefficient of nonlinearity are given in Equations 2.2 and 2.3:

$$\delta = \rho_0^{-1} \left[(\zeta + 4\eta/3) + \kappa \left(\frac{1}{c_v} - \frac{1}{c_p} \right) \right] \tag{2.2}$$

$$\beta = 1 + \frac{B}{2A} \tag{2.3}$$

Where ζ is bulk viscosity, η is shear viscosity, κ is thermal conductivity, c_v and c_p are specific heat at constant volume and pressure respectively and B/A gives a measure of the nonlinearity for the medium. The significance of B/A in acoustics lies in its relationship to the speed of sound which increases with particle velocity, and decreases with negative particle velocity. This variation in the speed of sound forms the basis of nonlinear acoustics summarized in Table 2.1.

Table 2.1 Typical B/A and attenuation values from [26]

Sample	B/A	Attenuation $\alpha\ (m^{-1})$ at 1 MHz	$c_0\ (\frac{m}{s})$ small signal sound speed
Water	5.0	0.017	1500
Human Blood	6.3	3.4	1580
Human liver	7.6	14.9	1570
Human fat	9.6	22	1460

The first term on the right hand side of Equation 2.1 accounts for diffraction, the second term for absorption and the third term for nonlinearity. The Sound waves are assumed to be parallel plane waves around z axis as shown in Figure 2.1. Local nonlinear effects due to source size and displacement are ignored.

With such an assumption the linear plane wave impedance Equation 2.4 can be used to describe the source condition in terms of sound pressure instead of normal velocity in the source plane .

$$p = \rho_0 c_0 u \tag{2.4}$$

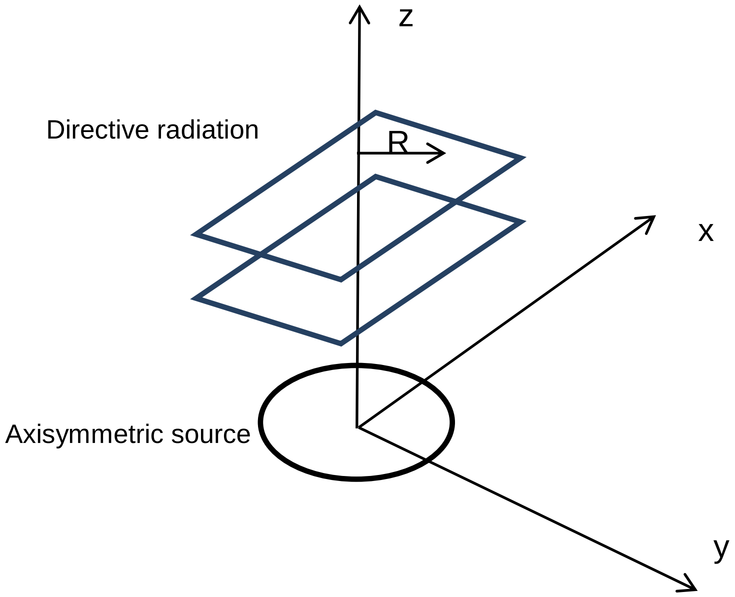

Figure 2.5 Geometry of radiation from axisymmetric sound source

Fully nonlinear analytical solutions of the KZK equation are not available at the present time, but linear, quasi-linear, and fully nonlinear without diffraction or without the nonlinear term are used to solve this differential equation. The Operator splitting method is a useful tool for numerical analysis and used in this thesis.

2.1.1. Operator splitting method

Operator splitting applies numerical techniques to each of the terms in the equation independently over a propagation step [25]. The KZK equation can be written in a non-dimensional format as

$$\frac{\partial^2}{\partial\sigma\partial\tau}P = \frac{1}{4G}\left(\frac{\partial^2 P}{\partial R^2} + \frac{1}{R}\frac{\partial P}{\partial R}\right) + A\frac{\partial^3 P}{\partial\tau^3} + NP\frac{\partial^2 P}{\partial\tau^2} \qquad (2.5)$$

With scaling parameters defined as

$$P = \frac{p}{p_0}, \qquad \sigma = \frac{z}{d}, \qquad R = \frac{r}{a}, \qquad \mathrm{T} = \omega_0 \tau \tag{2.6}$$

Dimensionless parameters defined as

$$G = \frac{z_0}{d}\ , \qquad N = \frac{d}{\overline{z}}\ , \qquad A = \alpha_0\, \overline{z} \tag{2.7}$$

With the parameters defined as

$$\overline{z} = \frac{\rho_0 c_0^3}{\beta p_0 \omega_0}, \qquad \alpha_0 = \frac{\delta \omega_0^2}{2c_0^3}\ , \qquad z_0 = \frac{\omega_0 a^2}{2c_0} \tag{2.8}$$

Where $\overline{z}$ is the plane wave shock formation distance from the pressure p_0, α_0 is the thermo viscous attenuation coefficient at a frequency ω_0 , and d is the characteristic focusing length. Parameter A in equation 2.7 should not be confused with parameter A defined in Equation 2.3 for nonlinearity. The parameters G,N,A respectively represent the small signal focusing gain, nonlinearity, and thermo viscous absorption. With the help of the new variables, the KZK differential equation can be rewritten as

$$\frac{\partial P}{\partial \sigma} = \mathcal{L}_D(P) + \mathcal{L}_A(P) + \mathcal{L}_N(P) \tag{2.9}$$

Where $\mathcal{L}_D$, $\mathcal{L}_A$ and $\mathcal{L}_N$ are the operators for diffraction, absorption and nonlinearity. The method of splitting operators applies the numerical methods sequentially at each propagation step with the step size of $\Delta\sigma$.

2.1.2. Linear part of KZK or Burger's equation

The equation which describes the propagation of the nonlinear progressive plane waves in a viscous medium in the z direction is obtained by neglecting the diffraction term in the KZK equation. This called Burger's equation.

$$\frac{\partial p}{\partial z} = \frac{\beta}{2\rho_0 c_0^3} p \frac{\partial p}{\partial \tau} + \frac{\delta}{2c_0^3} \frac{\partial^2 p}{\partial \tau^2} \tag{2.10}$$

The most useful and straight forward method for solving the linear part of this equation (e.g. Burger's differential equation) is using a frequency-domain technique. For each of the M harmonics considered in analytical solution:

$$p = \sum_{h=-M}^{h=M} \widetilde{p_h}(z)\, e^{jn\omega_0\tau} \tag{2.11}$$

$$\frac{\partial \widetilde{p_h}}{\partial z} + \frac{jc_0}{2} \nabla_\perp^2 \widetilde{p_h} + \alpha_h \widetilde{p_h} = 0 \tag{2.12}$$

Where $\widetilde{p_h}$ is the complex spectral amplitude and M is the number of harmonics considered. Substitution of Equation 2.11 in Equation 2.5 without considering the diffraction term, yields the ordinary set of differential equations as

$$\frac{\partial \widetilde{p_h}}{\partial z} + \alpha_h \widetilde{p_h} = jn\omega_0\beta_h \left(\sum_{m=1}^{h-1} p_m p_{h-m} + 2\sum_{m=h+1}^{M} p_m {p^*}_{h-m}\right) \tag{2.13}$$

Where ${p^*}_h$ is the complex conjugate of p_h, with ${p^*}_{-h}={p^*}_h$ because p is expected to be real. This first order differential equation can be solved numerically with the standard Runge-Kutta method.

2.1.3. The nonlinear part of KZK equation

After obtaining the linear solution for the KZK equation in the frequency domain, the solution can be converted to the time-domain using the fast Fourier transform. The Nonlinear part of the equation can be solved using the upwind method.

$$\frac{\partial}{\partial \sigma} P = NP \frac{\partial P}{\partial \mathrm{T}} \tag{2.15}$$

as described by Lee et al.,[27] the implicit solution of Burgers' equation can be described as:

$$P(\sigma, \mathrm{T}) = P_0(\mathrm{T} + NP\sigma) \tag{2.16}$$

By using linear interpolation an iterate method can be obtained as

$$P_i^{j+1} = \begin{cases} P_i^j \left[1 - N\left(\frac{P_{i+1}^j - P_i^j}{\Delta \mathrm{T}}\right)\Delta\sigma\right]^{-1} & \text{for } P_i^{j+1} \geq 0 \\ P_i^j \left[1 - N\left(\frac{P_i^j - P_{i-1}^j}{\Delta \mathrm{T}}\right)\Delta\sigma\right]^{-1} & \text{for } P_i^{j+1} < 0 \end{cases} \tag{2.17}$$

Here i and j represent the discretization in space and time, respectively. At each grid point, when the amplitude of the linear solution determined, the nonlinear consideration will be applied based on the amplitude obtained. This commonly used method for nonlinear hyperbolic conservation laws is called Godunov's scheme [28].

It is a generalization of the upwind differencing method for nonlinear problems consider as

$$P_i^{j+1} = P_i^j - \left(\frac{\Delta\sigma}{\Delta\tau}\right)\left[f_{i+1/2}^{j+1/2} - f_{i-1/2}^{j+1/2}\right] \tag{2.18}$$

Where f is called the flux for Burger's equation. For the nonlinear KZK equation this flux is defined as

$$f(P) = NP^2/2 \tag{2.19}$$

The Selection of amplitudes for Godunov's scheme as described before, will be made as [28]

$$f_{i+\frac{1}{2}} = \begin{cases} \dfrac{N}{2}\max\{P_i\,, \min(P_{i+1}, 0)\}^2 & \text{for} \quad P_i < P_{i+1} \\ \dfrac{N}{2}\max\,\{|P_i|\,, |P_{i+1}|\}^2 & \text{for} \quad P_i \geq P_{i+1} \end{cases} \tag{2.20}$$

2.1.4. Focused source and boundary conditions

The source initial condition at Z=0 can be modeled in different ways. Physical specification of the HIFU device such as inner or outer radius can be considered also. Several estimating function can be used including Error or Gaussian functions. The well-known [29] solution for source condition which is provided by the linear theory of diffracting beams, and has been used in this thesis, can be described as

$$P_0 = e^{-R^2}\sin(\,\tau + GR^2) \tag{2.21}$$

In the simulation procedure, the step sizes $\Delta\sigma$ and ΔR are determined at runtime by estimating the resolution requirements for a corresponding linear beam. To eliminate artifacts caused by reflection of waves from the unphysical boundaries of the computational domain, a perfectly matched layer (PML) absorbing boundary condition is implemented. The perfectly matched layer is located just outside the region of interest. PML converts propagating waves whose wavenumbers have nonzero radial components into decaying evanescent waves, absorbing them before they corrupt the solution. This technique allows the radial extent of the computational domain to remain small.

2.1.5. Frequency dependent parameters

The thermo-viscous attenuation coefficient defined in Equation 2.8 is a function of frequency. For better simulation of the ultrasound propagation in the medium the frequency dependent absorption in medium should be considered. This consideration is more important for frequency domain analysis that uses many higher harmonics above the fundamental. The attenuation coefficient versus frequency plays an important role in generating heat inside the medium [15] and defined as

$$\alpha(f) = \frac{2\delta\pi^2 f^2}{c_0^3} + \alpha_0\left(\frac{f}{f_0}\right)^\eta \tag{2.14}$$

2.1.6. Medium acoustic parameters

Material acoustic parameters for water and tissue mimicking material are extracted from previous research by Zell [31] and Maggie [30]. Parameters used in simulation are shown in Table 2.2.

Table 2.2 Acoustic parameters for water and tissue mimicking material

	Parameter	Symbol	Value	Unit
Water	small-signal sound speed	c_1	1482	m/s
	mass density	ρ_1	1000	kg/m^3
	absorption at 1MHz	α_1	0.217	dB/m
	exponent of absorption vs. frequency	η_1	2	--
	nonlinear parameter	β_1	3.5	--
	material transition distance	d	6	cm
Phantom	small-signal sound speed	c_2	1629	m/s
	mass density	ρ_2	1100	kg/m^3
	absorption at 1MHz	α_2	58	dB/m
	exponent of absorption vs. frequency	η_2	1	--
	nonlinear parameter	β_2	4.5	--

2.1.7. Bio heat transfer equation

The heat transfer in soft tissue during the thermal exposure to high temperature can be described using Pennes bioheat equation, which is based on the classical Fourier law of heat conduction .The Pennes model is used to address the heat transfer in living tissues. The model is based on the assumption of the energy exchange between the blood vessels and the surrounding tissues. Even though there may exist some differences in describing bioheat transfer in regimes where vascular countercurrent heat exchange can possibly skew heat flux and temperature information, Pennes' model may provide suitable temperature distributions in whole body, organ, and tumor analysis under study [32].

According to Pennes' model, the total energy exchange by the flowing blood is proportional to the volumetric heat flow and the temperature difference between the blood and the tissue. The three-dimensional expression of Pennes' bioheat equation in a media with uniform material properties to determine temperature is given by

$$\rho C \frac{\delta T}{\delta t} = k\nabla^2 T + H - wCT \tag{2.15}$$

Where ρ is tissue density (kg/m^3) , C is heat capacity or specific heat (J/kgK), H is heating rate (W/m^3) , w is perfusion rate (kg/m^3 s) and k is thermal conductivity (W/mK).

One benefit of computing the solution in both time and frequency domains is that information is easily accessed from both. After computing the harmonic component of wave pressure in a medium, the spatial distribution of intensity and heating rate can be computed using the plane wave approximation

$$I(r,z) = \frac{1}{2\rho c}|P(r,z)|\,, \qquad H(r,z) = \frac{\alpha}{2\rho c}|P(r,z)| \tag{2.16}$$

The result of the KZK numerical solution can be used to determine the heating rate in Equation 2.16. The Bio Heat differential Equation (BHT) is commonly solved with a second order finite difference discretization. Because the boundary condition (ambient temperature) gives value to the solution, Dirichlet boundary conditions should be used.

2.1.8. Medium heat transfer parameters

Heat wave related parameters for water and tissue mimicking material are extracted from previous research by Shenn et al. [22]. Parameters used in simulation are shown in Table 2.3.

Table 2.3 Temporal parameters for water and tissue mimicking material

	Parameter	Symbol	Value	Unit
Water	heat capacity thermal conductivity perfusion rate	c_1 k_1 w_1	4180 0.6 0.0	J/(kgK) W/(mK) Kg/m^3 s
Phantom	heat capacity thermal conductivity perfusion rate	c_1 k_1 w_1	4180 0.6 20	J/(kgK) W/(mK) Kg/m^3 s

CHAPTER 3

SIMULATION PARAMETERS AND RESULTS

3.1 Simulation Parameters

Simulation was performed with MATLAB-r2010b on Dell computer with Intel Core Duo 3.0 GHz processor and 4 GB RAM. Four sets of simulation were performed for configuration shown in Figure 3.1 and three power levels of 10, 25, 56 and 100 watts were applied. Simulation starts with setting the initial parameters and calculating the initial pressure on the HIFU plane.

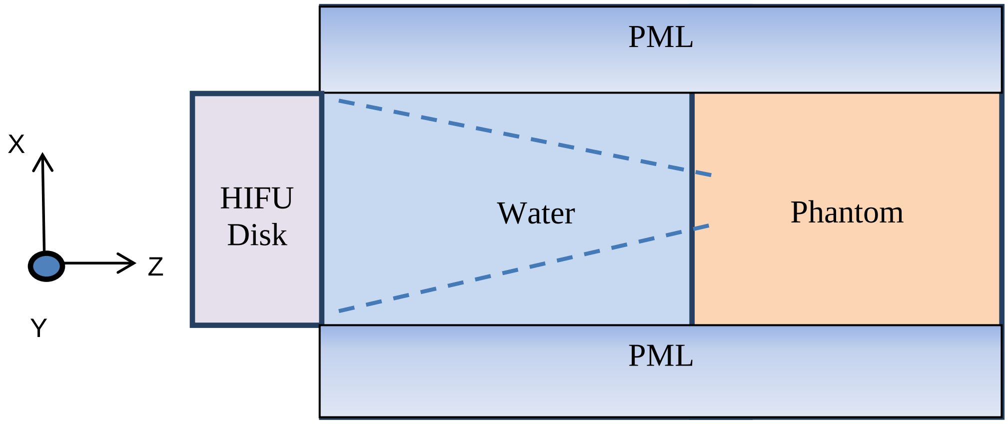

Figure 3.1 Geometric configuration of numerical analysis, HIFU radius=2.5cm, water layer length =5cm and phantom layer length=5cm

Initial excitation at the HIFU plane is assumed to have a Gaussian distribution and phase shift with respect to focusing depth. Initial condition on a surface of the HIFU considered as

$$P_0 = e^{-R^2} \sin(2\pi\, f + GR^2) \tag{3.1}$$

A perfect matched layer placed around the radial perimeter of the HIFU to absorb all unwanted distortion from boundaries. Other initial parameters are also shown in Table 2.2 and Table 2.3 .

Frequency of operation is 2.5 MHz (period of 0.4 microseconds). The HIFU diameter is set to 5 cm and 32 harmonics are considered in the simulation. This initial sinusoidal pressure wave starts from the HIFU plane and propagates in the Z- direction through the water for 6 cm, then enters the phantom and continues for another 6 cm. As the wave propagates through the nonlinear medium it becomes distorted as shown in Figure 3.2.

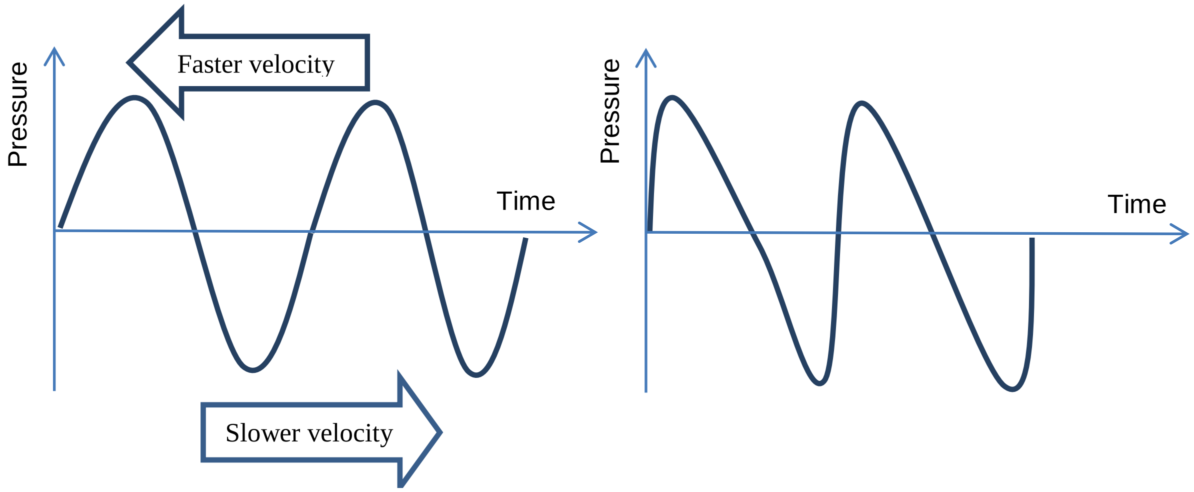

(a) (b)

Figure 3.2 The impact of nonlinear propagation with propagation distance due to the amplitude dependence of wave velocity. a) Sinusoidal wave at source b) nonlinear distorted wave at distant.

3.2 Simulation Results

For each input power of 10, 25, 56, and 100 watt, initial pressures of 0.13, 0.21, 0.32 and 0.42 MPa are obtained respectively. Maximum intensity of pressure wave inside the phantom has happened at z = 6.8 cm. This point is called the focus point and is considered as an important point to show pressure wave signal versus time inside the phantom as shown in Figure 3.3. One should notice that the time axis in this set of graphs starts at t=0 which means the time delay is not considered. The actual time that a pressure wave takes to pass through 6 cm of water and 0.8 cm of tissue mimicking material to reach the focal point at z=6.8 is actually 7.6 microseconds.

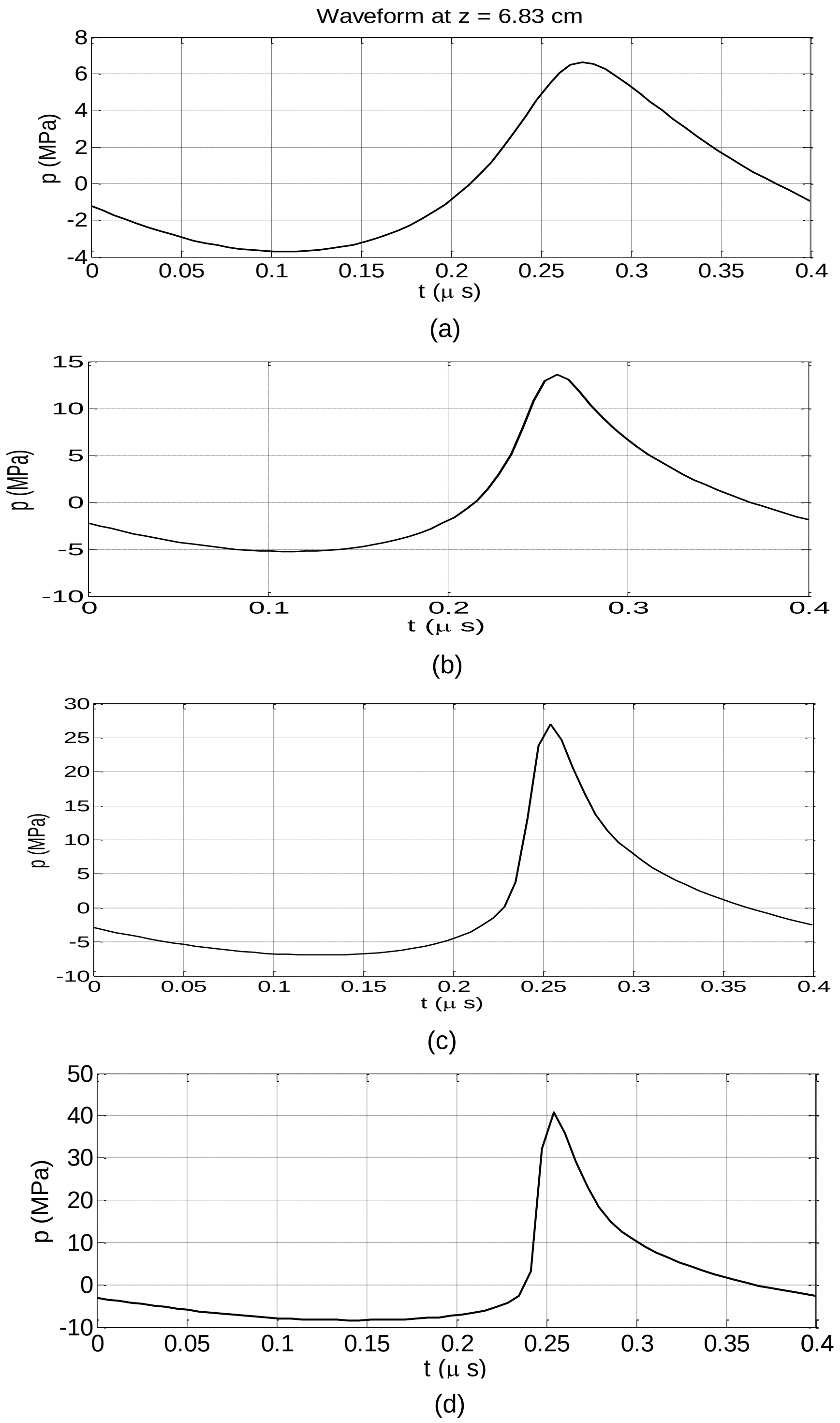

Figure 3.3 Pressure wave vs. retarded time at axial distance of z= 6.83 cm from center of HIFU for different powers of a) Pin=10 W b) Pin =25 W c) Pin=56 W d) Pin=100W

For each input power of 10, 25, 56, and 100 Watt, the axial distribution of intensity and heating rate are computed using the plane wave approximation as

$$I(r,z) = \frac{1}{2\rho c}\sum_{h=1}^{32}|\widetilde{p_h}| \ , \qquad H(r,z) = \frac{1}{2\rho c}\sum_{h=1}^{32} Re(\alpha_h)|\widetilde{p_h}| \tag{3.2}$$

The pressure wave components are calculated with solving the Burger's equation

$$p = \sum_{h=-32}^{h=32} \widetilde{p_h}(z)\, e^{jn\omega_0\tau} \tag{3.3}$$

$$\frac{\partial\widetilde{p_h}}{\partial z} + \frac{jc_0}{2}\nabla_\perp^2\widetilde{p_h} + \alpha_h\widetilde{p_h} = 0 \tag{3.4}$$

The results of calculation are shown in Figure 3.4 for Intensity versus axial distance z from the center of the HIFU. Figure 3.5 shows the calculation results of axial heat rate in the Z direction from the center of the HIFU. The five first harmonics of pressure waves in the axial distance from center of the HIFU are also shown in Figure 3.6. This figure shows how different components of pressure wave changes versus input power. As the input power increases nonlinear effects are increasing significantly. Simulation results shows that ratio of peak pressure intensity of the first harmonic over the third harmonic decreased to 9, 7, 4 and 2.5 with respect to the input power increase to 10, 25, 56 and 100 Watt, respectively.

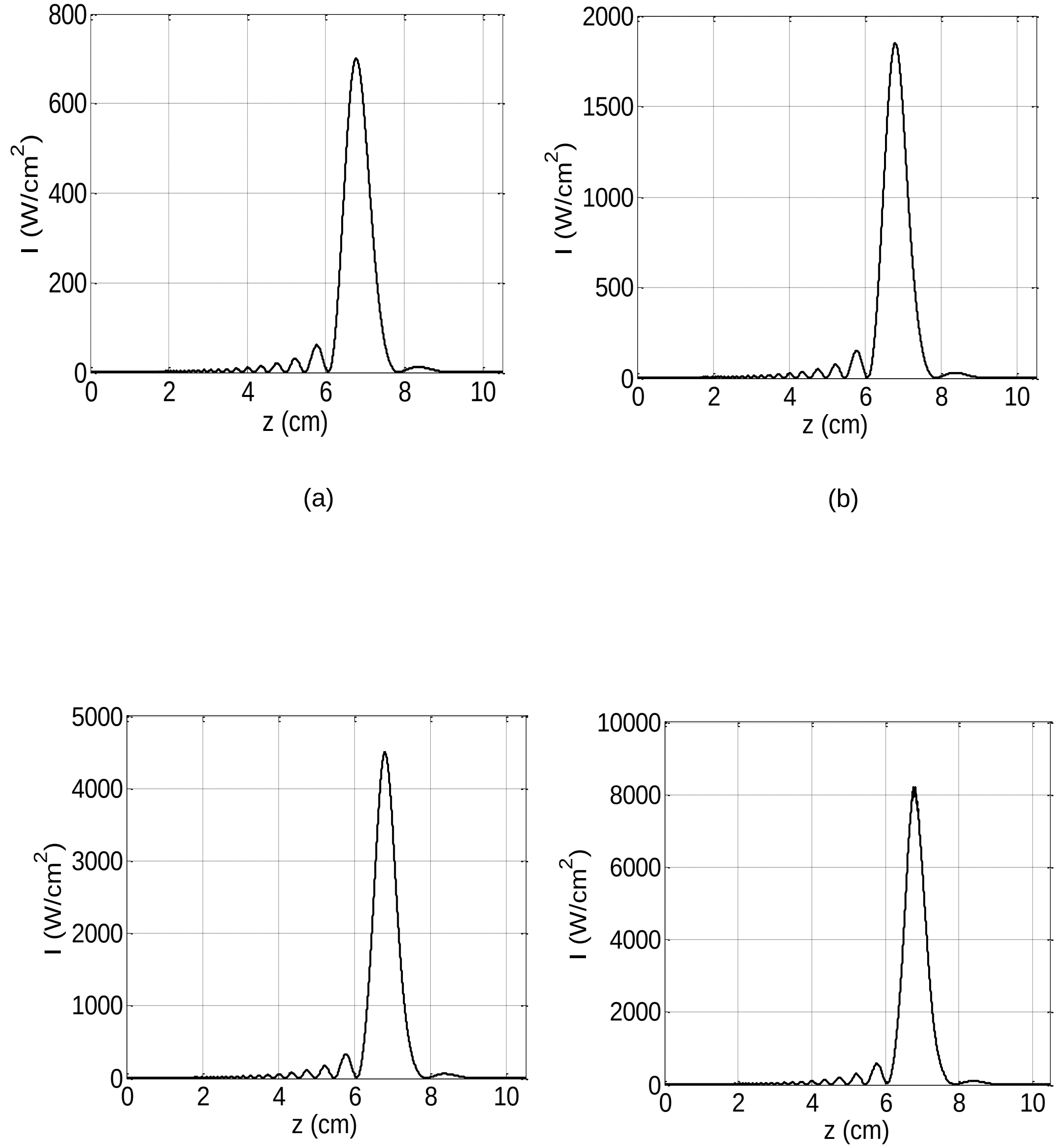

(a)

(b)

(c)

(d)

Figure 3.4 Simulation results for intensity vs. axial distance from center of HIFU for a) Pin=10 W b) Pin =25 W c) Pin=56 W d) Pin=100 W

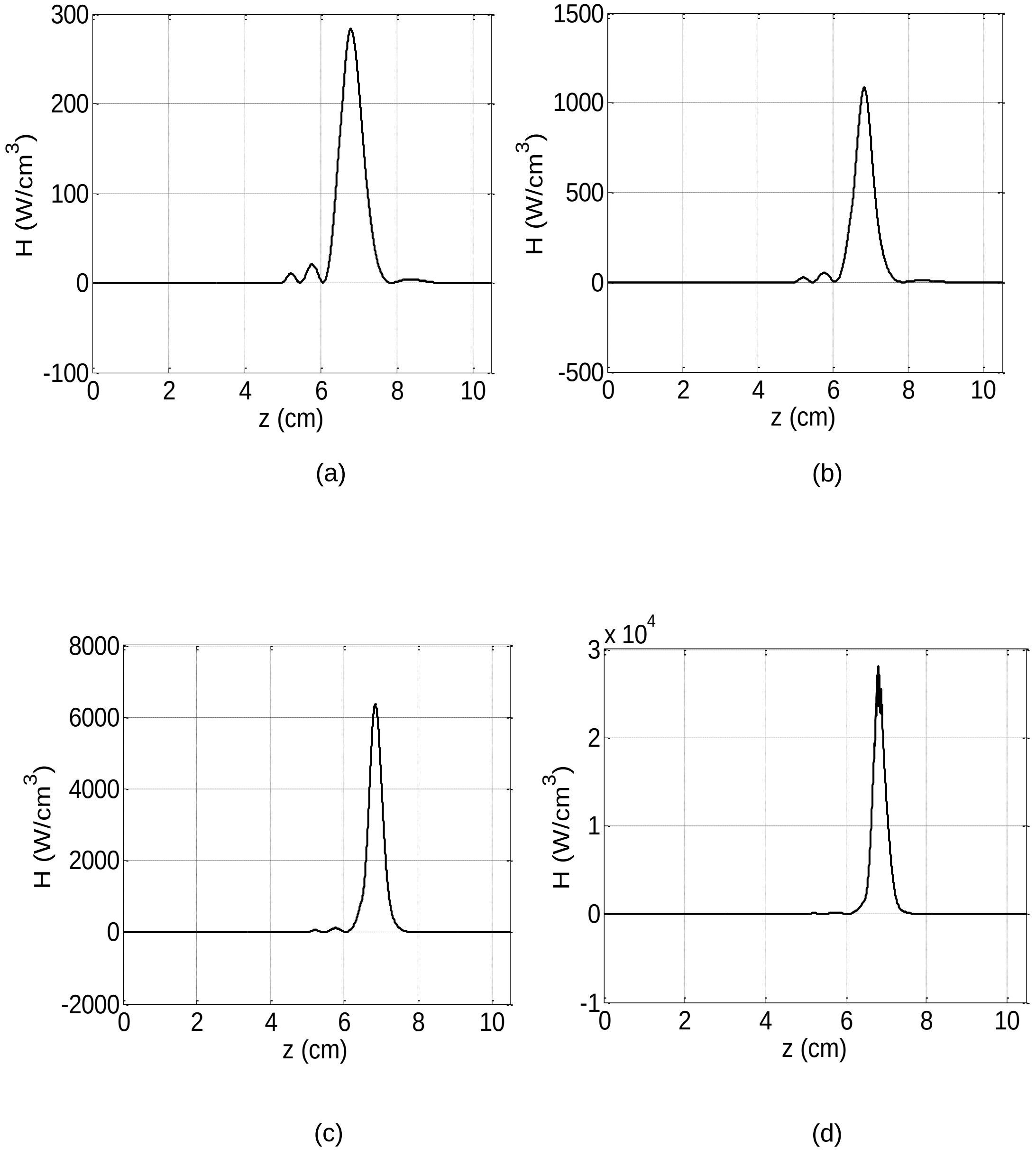

(a)

(b)

(c)

(d)

Figure 3.5 Simulation results for heat vs. axial distance from center of HIFU for a) Pin=10 W b) Pin =25 W c) Pin=56 W d) Pin=100 W

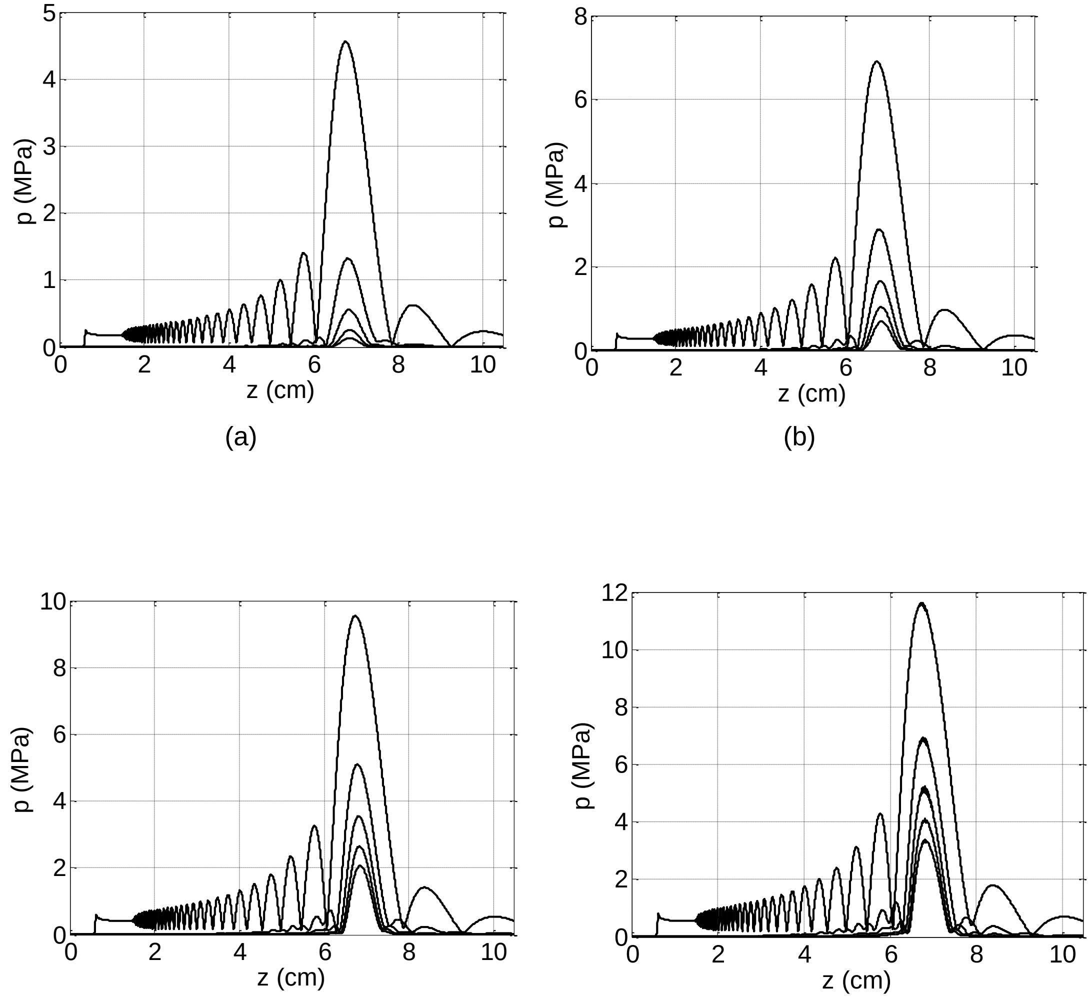

(a)

(b)

(c)

(d)

Figure 3.6 Simulation results for five first harmonics of pressure vs. axial distance from center of HIFU for a) Pin=10W, b) Pin =25 W c) Pin=56 W d) Pin=100 W

To determine the temperature rise and distribution, the Pennes' Bio Heat Transfer (BHT) equation is used

$$\rho C \frac{\delta T}{\delta t} = k\nabla^2 T + H - wCT \tag{3.5}$$

A second order finite difference discretization is used and the solution is evolved in time using a second-order Runge Kutta method. H is the heating rate calculated in previous steps of solving KZK equation. The excitation of pressure waves usually has much higher frequency than the switching rate of the HIFU. For example in this thesis the operation frequency of the HIFU is 2.5 MHz while it is considered to be excited with a pulse by the specification shown in Figure 3.7. Since the duty cycle of this excitation pulse is 10%, it can be assumed that this condition is the equivalent of 10% of actual used in previous simulation for continuous sinusoidal wave power. In all the illustrations the small time delay between excitation and temperature measurement is ignored and the time scale is assumed to start from t=0. This time delay is in order of microseconds for 6 cm of water and 0.8 cm of phantom as explained before and can be neglected with respect to time scales of millisecond excitation.

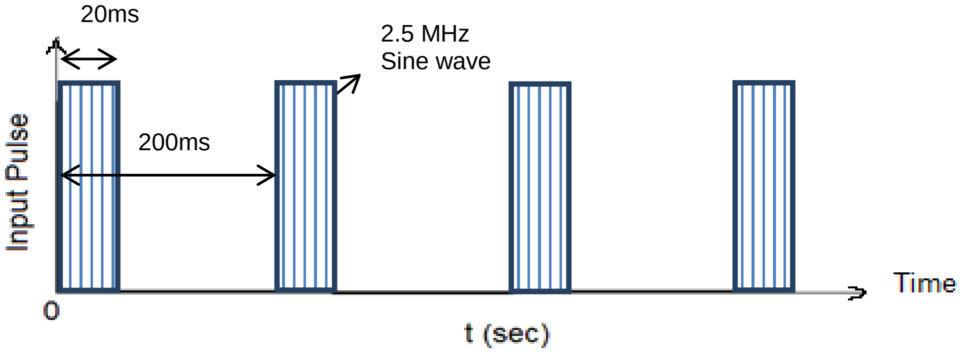

Figure 3.7 Input excitation pulse for the HIFU

Five pulse of excitation as shown in Figure 3.7 is applied and the temperature increase due to this excitation calculated and shown in Figure 3.9 for input powers of 10, 25, 56 and 100 Watt.

In another simulation, the same heating excitation is considered for 0.35s (or 5 pulse of 70ms) continued by one second of cooling to analyze the cooling effect of the simulated tissue. Results of this simulation are shown in Figure 3.10 for input powers of 10, 25, 56 and 100 Watt. In order to visualize the heating effects inside the tissue mimicking material contours of equal temperatures are calculated in the axial plane of HIFU (known as focal plane) as shown in figure 3.9. These contours show the temperature in the r-z plane passing from the center of the HIFU in axial direction of z. results of these calculations are shown in Figure 3.12. Maximum temperature occures after the 5th pulse applied at the time t= 0.82 s because 800 ms (or 4x200 ms) was required for the first 4 pulses plus 20 ms ON time of the fifth pulse. All contours are plotted at t=0.82 s when the maximum temperature occurs.

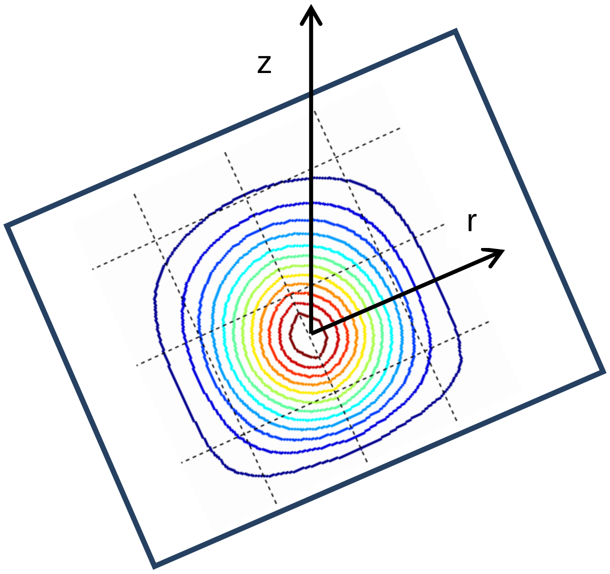

Figure 3.8 Demonstration of temperature contour plane passing from focal point

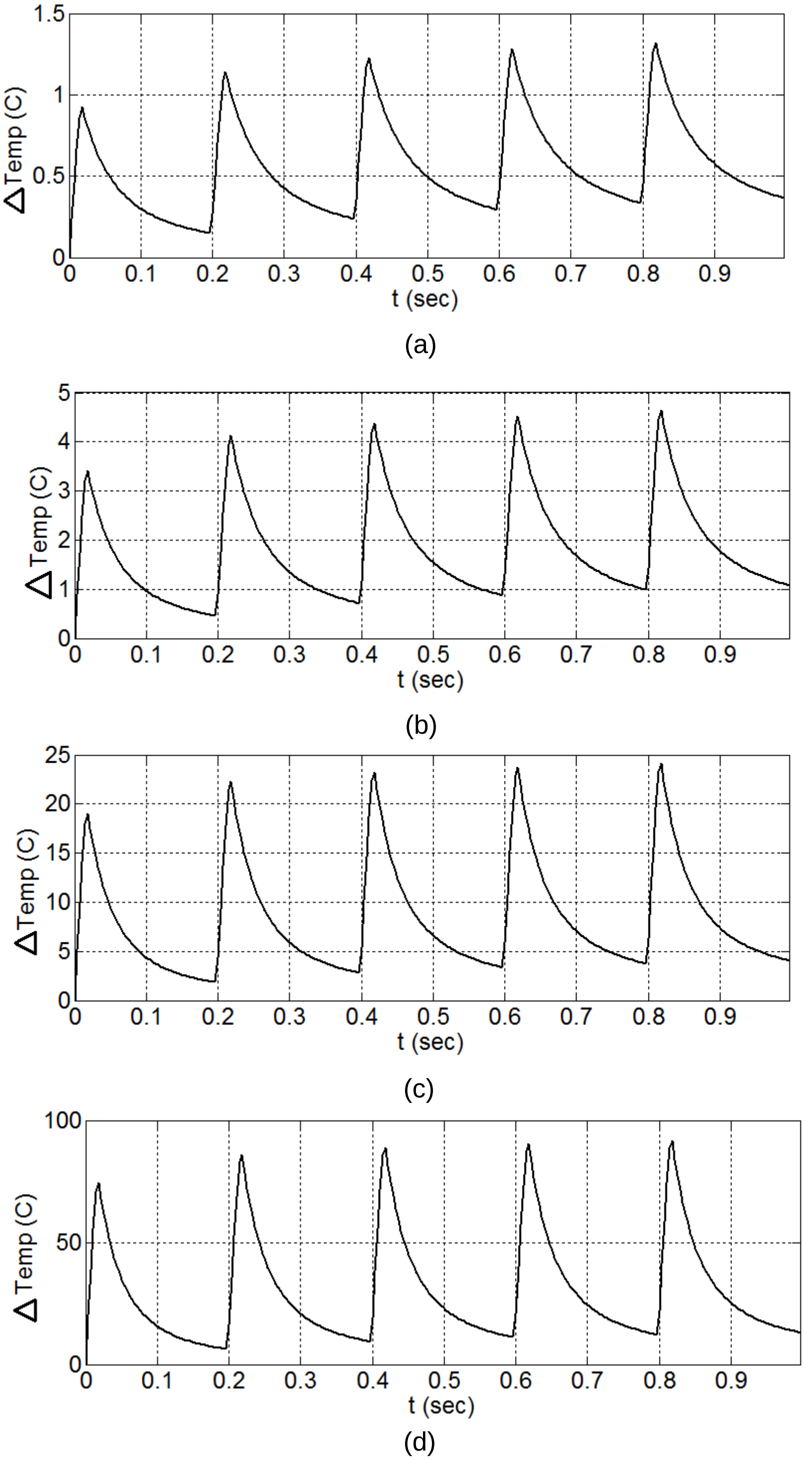

Figure 3.9 Simulation for temperature variation vs. Time in response to five input burst of 20ms ON and 200ms OFF (9% duty cycle) for the input power of
a) 10W b) 25W c) 56W d) 100W

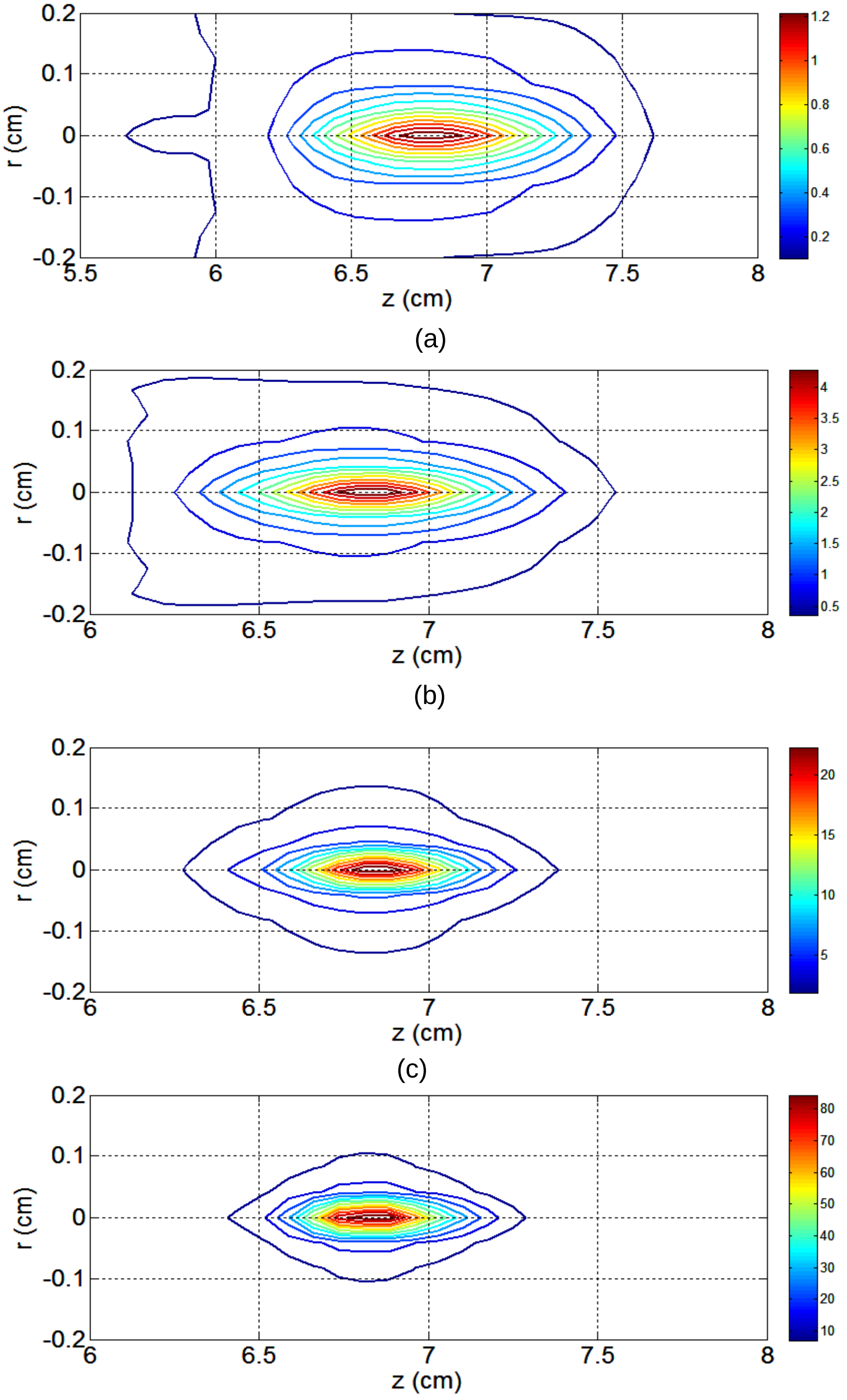

(a)

(b)

(c)

(d)

Figure 3.10 Temperature distribution contour at focal point in r-z plane. All contours are plotted at maximum temperature at t= 0.82 s in response to input burst of five 20ms ON and 200ms OFF (9% duty cycle) pulses with the input power of a) 10W b) 25W c) 56W d) 100W

Each simulation run using MATLAB took about 11 minutes for KZK and 20 minutes for BHT. Timing steps are shown in Appendix 1 and MATLAB codes for the KZK and BHT differential equations can be found in Appendix 2.

CHAPTER 4

EXPERIMENT METHOD AND RESULTS

4.1 Experiment Setup

The equipment consisted of a water tank filled with degassed tap water. Three positioners were attached to an external enclosure to provide three axis positioning of the transducer. The infrared camera (FLIR SC6000 InSb) was attached to an aluminum stand and fixed with screws on top of the optic table. The camera was placed on top of the tank with cables and power supply connected to its inputs. This allowed for adjusting the height of the IR camera such that the sample holder was in its field of view. Right angle clamps were used to position the HIFU transducer in water. Micrometer stands were used to adjust the distance between the HIFU and sample holder. Function generator was connected to power amplifier and matching network to provide Ultrasonic excitation for the transducer. A camera was connected through a 1Gb/s Ethernet cable to computer using FLIR's ExaminIR version 1.30.0 (Build 72 February 17, 2011) software to control the camera, capture video and extract thermal data. Figure 4.1 is the schematic of the setup used.

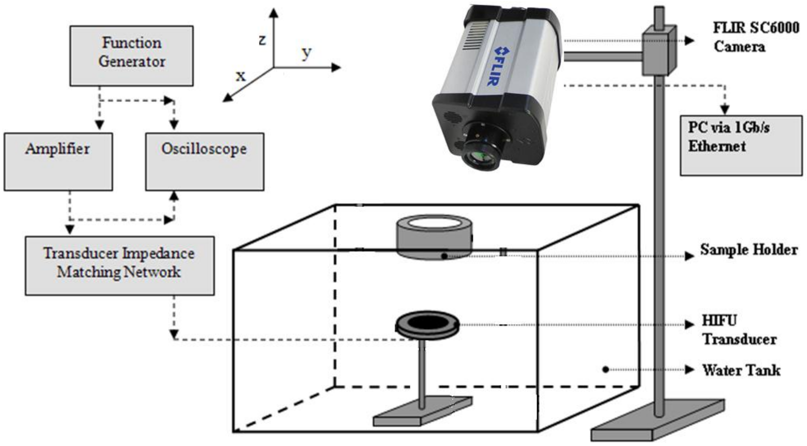

Figure 4.1 Experiment equipment and setup

The Sonic Concept® H108 transducer with outside diameter of 6 cm, focal length of 5 cm was used. The Tissue Mimicking Material (TMM) was produced using VST 50 silicone elastomer and was sliced with a sharp knife into two centimeter width and placed inside the sample holder above the water surface. Because the IR camera sees through the outside layer of the TMM, the flatness of the surface is very important in this experiment. The tank was filled with fresh de-gassed water. The function generator was set to produce a pulsed burst signal with a carrier 2.5 MHz frequency. The duty cycle of the burst was adjusted to 20 ms ON and 200 ms OFF cycles. The transducer, sample holder and camera were aligned such that they were in a straight line, as shown in Figure 4.2. The focus of the IR camera was checked and adjusted if necessary. The Infrared camera was adjusted for 128x128 pixel window size, integration time of 200 microsecond, and a frame rate of 1000 FPS. Temperature nonlinearity calibration and bad pixel detection was performed based on the provided manufacturer data.

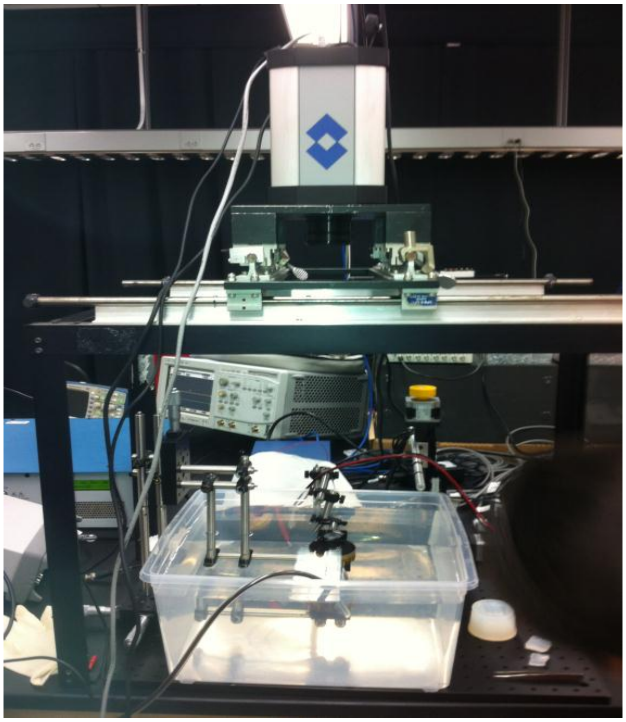

Figure 4.2 HIFU, Infrared camera and sample holder alignment setup

4.2 Data Acquisition

The ExaminIR® Region of Interest (ROI) tool was used to collect the temperature versus time variation from the video stream. A circular type ROI was defined at the center of the image with a radius of 4 pixels where the maximum heating at focal point observed. The actual size of the TMM was 2cmX2cm. The lens of the camera was adjusted to have the best focused picture. The distance of the camera from the sample was also adjusted to 30cm to have the complete view of 128X128 pixels sample. Each pixel of the picture in this adjustment represents 156 micrometers on the sample. Line ROI shown in Figure 4.3 was also used to collect the spatial temperature distribution on the surface. Line ROI was defined from one side to side of the picture passing through the center of the image and covered all 128 pixels. Circular ROI is shown in Figure 4.3. The resolution of this figure retained 128 pixels in order to show the actual condition. The voltage level of the function generator was set to achieve the required power levels at the output of the power amplifier. All the input powers shown in data are calculated based on 50 Ohms input impedance assumption for the HIFU. The duty cycle of the waveform was set by adjusting the function generator. An ultrasound wave applied for three different powers, and a long term heating and cooling profile was recorded to investigate the heating and cooling behavior of the sample.

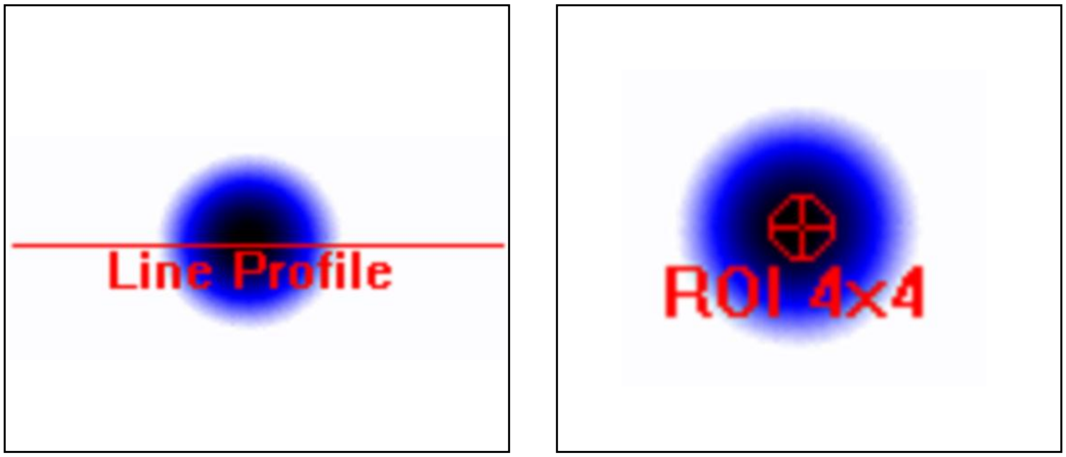

(a) (b)

Figure 4.3 ExaminIR® thermo graphic analysis tool a) Line profile b) Circular ROI

Figure 4.4 shows the result of long term heating and cooling measurement. This measurement shows the final pixel intensity versus time. Heating period was performed continued 40 seconds for the 25 W, 30 seconds for 56 W and 60 seconds for 25 W input powers. The source turned off after this heating period, and the video capturing continued for the cooling period. Each run of the experiment generated a very large amount of data because of the high frame rate of 1000 per second. Figure 4.4 shows that the heating profile for all three powers has linear behavior and it was the motivation to choose the 5 period required to show the short term variation of pulse heating. The IR camera temperature calibration information versus pixel intensity for the window size of 128 pixel and integration time of 200 microseconds is also shown in Table 4.1.

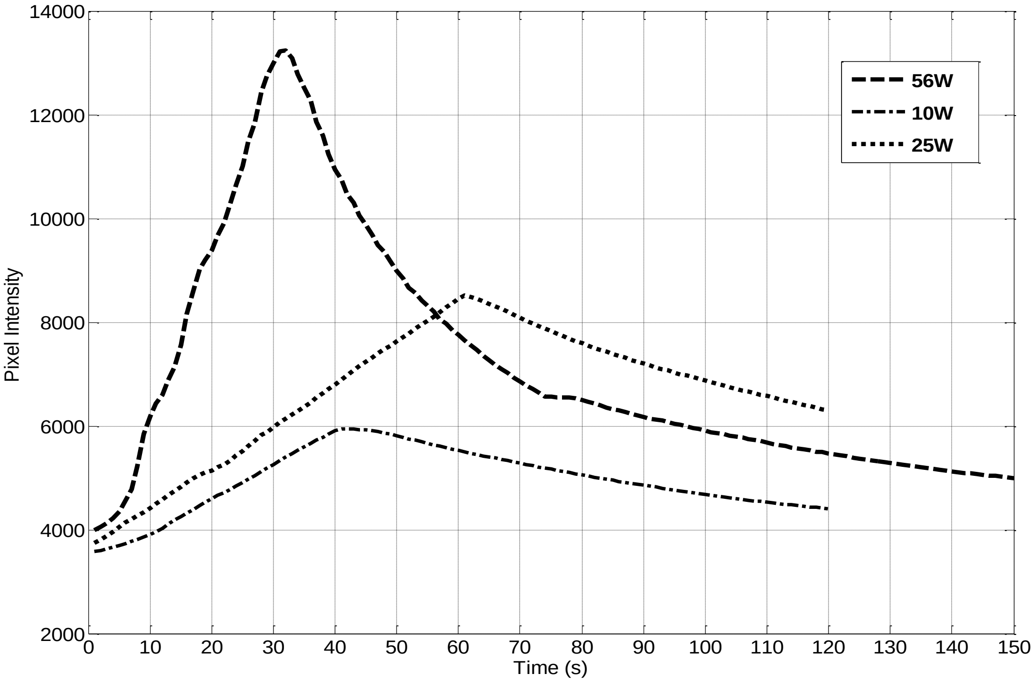

Figure 4.4 Heating and cooling profile vs. time for different input powers

The boiling point of the tissue mimicking material was not precisely known, but it was between 90 and 100 °C. The final temperature of the TMM was kept below the boiling point of the TMM. The IR camera recording was started to capture the developing heating pattern on the TMM surface. Three power levels of 10, 25 and 56 Watt were applied and the transducer was switched off after each run to let the TMM cool down to room temperature.

Table 4.1 Pixel intensity vs. temperature calibration

Temperature	20	25.8	30.4	34.2	40.6	45.8
Pixel Intensity	4,000	6,000	8,000	10,000	12,000	14,000

Temperature data was obtained for three different power levels and streaming video of 1000 frames per second was captured. In the ExaminIR® software the high frame rate video stream was recorded in the file, but only the sampled frame rate of 5 Hz were shown on the monitor due to graphic card and monitor limitation for frame rate. In order to show the online streaming video, there is an option in the software that skips some frames. This option in video capture setting was unchecked to make sure all the frames were being captured.

The motivation of choosing 128 by 128 pixel window was to achieve the 1000 frame per second sampling rate and ability to capture the amount of data through the commercial 1Gb/s Ethernet connection. The window size of the video can increase to 600 by 800 pixels and each pixel contains 12 bits of data. Not only the frame rate will dramatically decreases by such high resolution but also special Ethernet interface is required to transfer the amount of data in real time.

In order to show the effect of heating and compare the experimental results with simulation, only 5 burst pulses were required. Video frames from 25 second to 26 second of the 120 second complete record (60 seconds heating and 60 seconds cooling) were used. The video stream was stopped at 10 second, with three steps of ten seconds. Results are shown in Figure 4.5 to 4.7. The axial focal point of the HIFU is completely clear in these frames. The line profile can detect the hot spot of the frame window which is the axial axis of the focal point.

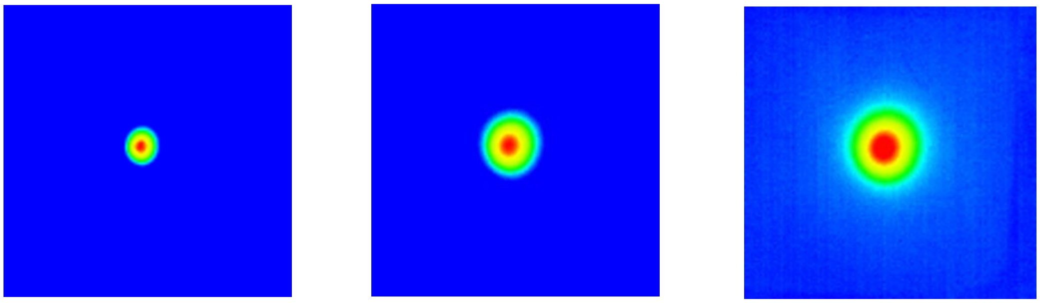

(a) (b) (c)

Figure 4.5 Extracted pictures from video IR camera video stream for 10 W input power in three time steps of a) 10 s b) 20 s and c) 30 s

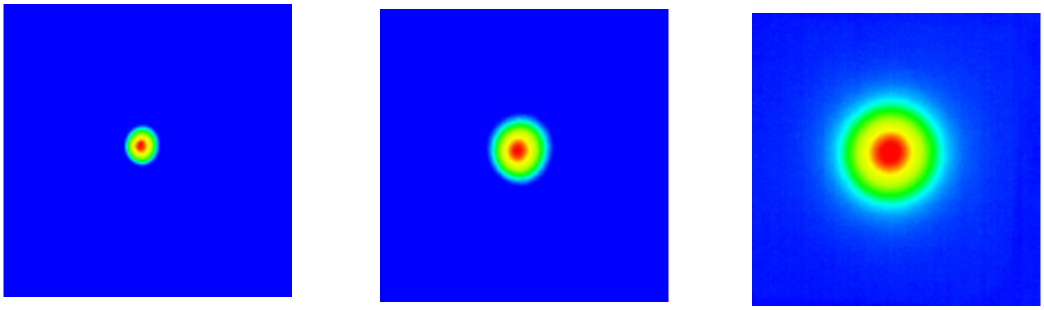

(a) (b) (c)

Figure 4.6 Extracted pictures from video IR camera video stream for 25 W input power in three time steps of a) 10 s b) 20 s and c) 30 s

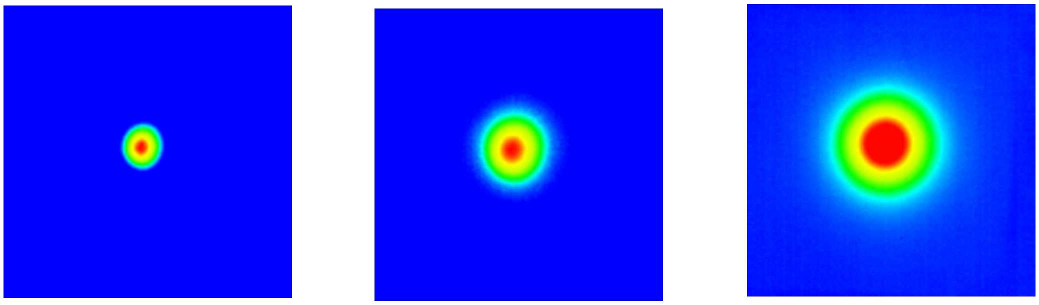

(a) (b) (c)

Figure 4.7 Extracted pictures from video IR camera video stream for 56 W input power in three time steps of a) 10 s b) 20 s and c) 30 s increase. In order to measure the spatial distribution of the temperature, line profile ROI was applied. In the first few experiment runs, the spatial distribution was not similar to the expected distribution.

The tilted sample at the sample holder or non-even TMM surface can alter the spatial measurement results. An uneven surface was avoided by slicing the TMM to the desired length with a sharp cuter. The sample holder was also kept at the horizontal level. Since the TMM is floating on top of the water level, its surface should be kept dry and free from tiny water drops that can occur during adjustments or filling the tank. Spatial distribution shows the normalized temperature spread through the line profile ROI for each pixel from side to side of the view. It passes from the axial focal point of HIFU where the maximum temperature occurs. The effect of false measurements due to surface roughness and a tilted sample are shown in Figure 4.8 and Figure 4.9 respectively.

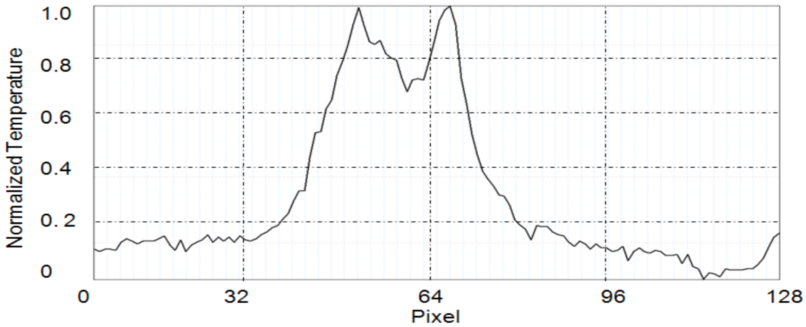

Figure 4.8 False measurement due to TMM surface roughness

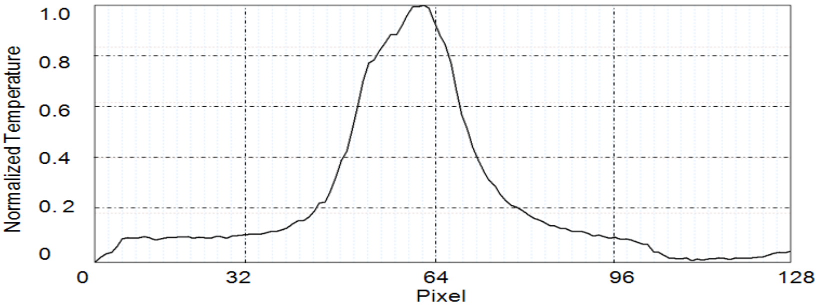

Figure 4.9 False measurement due to tilted TMM surface

Spatial distribution of the heating effect was measured for three input powers of 10, 25 and 56 W. Normalized temperatures versus pixel numbers are shown in Figure 4.8 to Figure 4.9. The left lower side of the picture window was assumed to be the origin (0,0) and top right of the window was (128,128). The horizontal ROI line profile was used to obtain this data was started at (0, 64) and ended at (128, 64) which passes from the center of window.

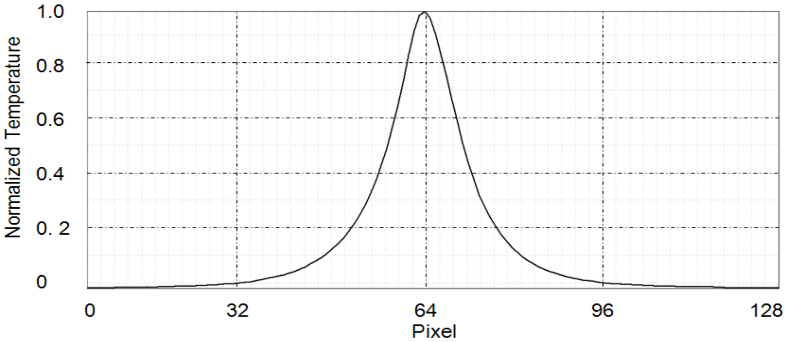

Figure 4.10 Normalized temperature distribution from point (0,64) to (128,64) for 10 W input power

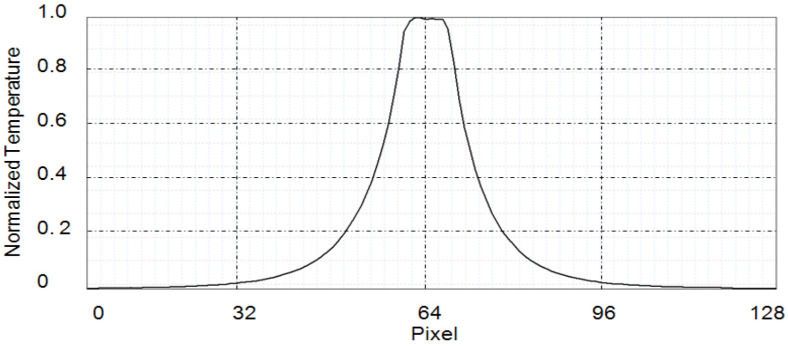

Figure 4.11 Normalized temperature distribution from point (0,64) to (128,64) for 25 W input power

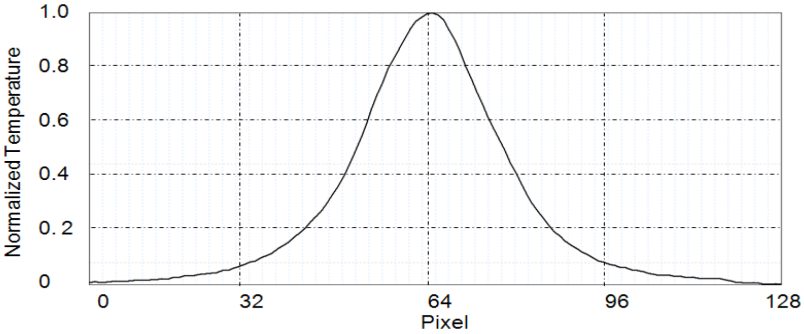

Figure 4.12 Normalized temperature distribution from point (0,64) to (128,64) for 56 W input power

Circular ROI with radius of 4 pixels at the center of the image were used to obtain time transient temperature data for three input powers of 10, 25 and 56 W. Frames from 30 second to 31 second of video stream were used to extract the figures to show the effect of five 200ms Ultrasound burst. Results are shown in Figure 4.13 to 4.15 for each input power.

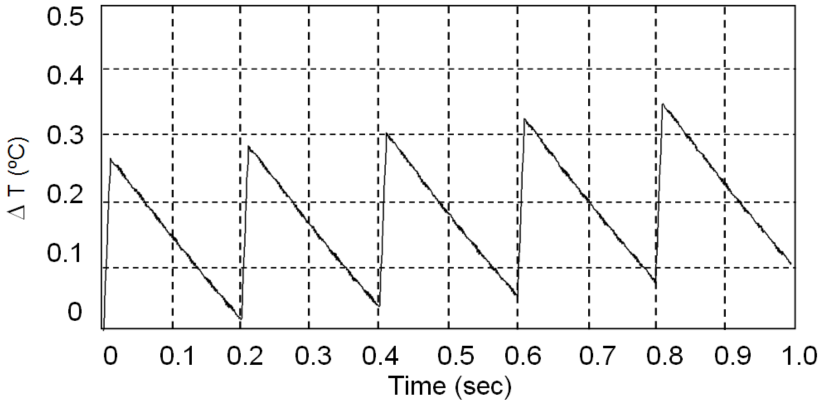

Figure 4.13 Temperature variation vs. time (after t_0=20s) for 10 W input power

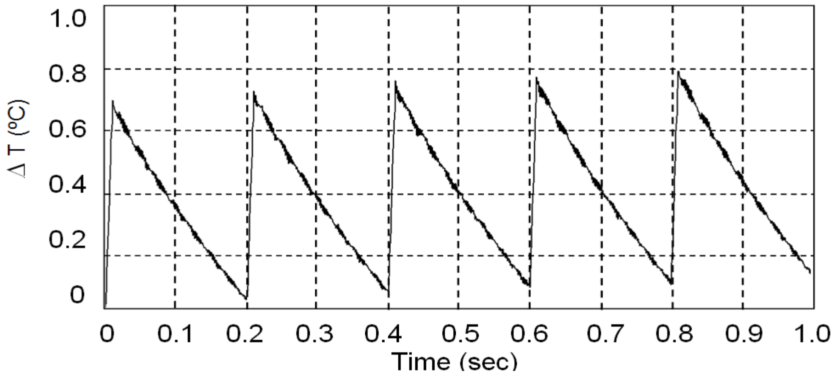

Figure 4.14 Temperature variation vs. time (after t_0=30s) for 25 W input power

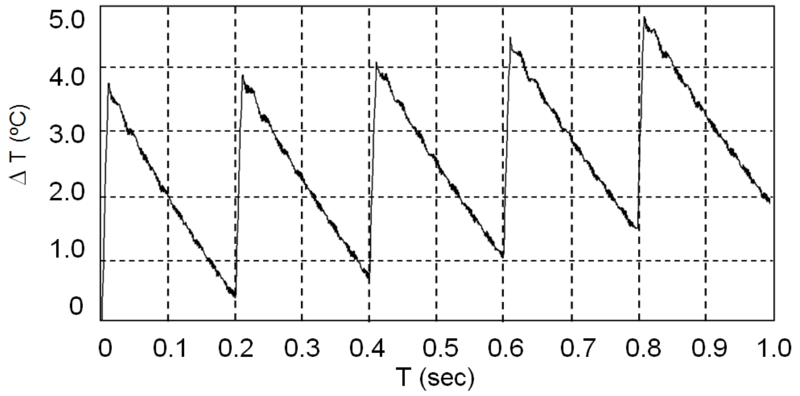

Figure 4.15 Temperature variation vs. time (after t_0=30s) for 56 W input power

4.3 Summary and Discussion

Infrared measurements of temperature were made at the 3 transducer powers. Spatial distribution, temperature variation versus time measurements were applied using the line ROI and circular ROI tools. The Infrared measurement method can be used to determine the focal point in axial location of the unknown HIFU. The hot spot or focal axial point of the HIFU can be detected by selecting the circular type ROI defined at the center of the image.

In this study a 128 by 128 pixel window shows the entire 2 cm x 2 cm phantom and the accuracy of each pixel is around 160 micrometers. The focal point of H-108 Sonic Concept ® HIFU used in this study was 500 micrometers. The ROI was set to be circular and holding 5 pixels at the center of the image. (The 2 pixels radius and center point form the 5 pixels circle). The average of these 5 pixels was used to determine the pixel intensity and temperature for both transient and long term sonication. The heating and cooling behavior of each pulse with different powers are compared in Table 4.2. This table shows that results from measurement and simulation are correlated with the constant ratio of the temperature increase per second. Although the VST 50 silicone material is semi clear and allows the infrared camera to see radiation from the inside, this temperature was measured from 30 cm axial distance from the phantom on the surface.

Measured temperature curves were significantly different from simulation. In the simulation result the heating and cooling curves are exponential while in the measurement with the IR camera the wave forms are saw tooth. By setting the standard for the phantom material specification, the IR camera and axial distance of the measurement it is possible to estimate the power and focal length of the unknown HIFU with this method. Another extension of the present work that has important practical impact is to determine the intensity distribution in the absence of the air interface. In clinical applications of the HIFU, the air interface will not be present, and it is useful to relate the intensity measured by the IR camera and the physiological situation. With the air interface present, the total acoustic intensity consists of a term due the incident beam, and reflected beam from interface

Table 4.2 Comparison of the IR measurement from 30cm and simulation result

Input Power	Pulse #	ΔT after each pulse from				Temperature Increase / s	
		Measurement		Simulation		Measurement	Simulation
		Inc	Dec	Inc	Dec		
5Watt	1	0.25	0.24	0.8	0.6	0.11	0.4
	2	0.26	0.23	0.8	0.7		
	3	0.25	0.24	0.8	0.7		
	4	0.25	0.23	0.8	0.75		
	5	0.27	0.24	0.8	0.75		
25 Watt	1	0.75	0.65	3.2	3.0	0.25	0.8
	2	0.75	0.65	3.2	3.1		
	3	0.75	0.65	3.2	3.1		
	4	0.75	0.65	3.2	3.1		
	5	0.75	0.65	3.2	3.1		
56 Watt	1	3.8	3.6	17	15.5	1.1	4.0
	2	3.8	3.6	16	15.5		
	3	3.9	3.6	16	15.5		
	4	3.8	3.6	16	15.5		
	5	3.8	3.6	16	15.5		

It is likely that the interference field, which varies rapidly in space, cannot be ignored, especially when a thinner phantom is used. Furthered development in simulation and study of the governing differential equation is required to consider the effect of thin phantom instead of semi-infinite phantom that was used in this thesis. The pressure wave intensity near the air layer is at maximum and generates the maximum temperature at the focal point. It is more likely that the air layer on top of thin phantom decreases the heat conductivity and keeps the inner layer temperature inside the phantom. This blocking to normal heat transfer increases the exponential rate of cooling and heating. One possible solution for this problem is to run the simulation for the KZK with the same parameters and decrease the heat conductivity in the BHT simulation to compensate for the air layer. Another consideration is to decrease the duty cycle of the pulses. Very small duty cycles of the exciting pulse can force the time step in simulation to very small numbers and working with very small and very large numbers in time difference method can increase the computation errors.

Another set of simulation was run based on the above consideration with a 50% decrease in the phantom heat conductivity and the result for 56 W input power is shown in Figure 4.16.

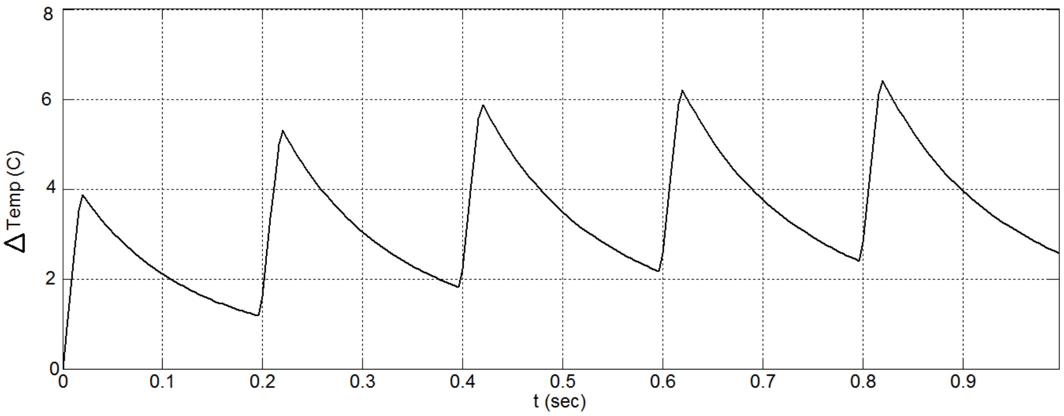

Figure 4.16 simulated temperature vs. time with 20% phantom heat conductivity decrease for compensating the air layer

As it is shown in Table 4.2 simulation and experimental results are different with a multiplier of 4 with 10% accuracy. This difference is mostly coming from the fact that IR camera measurements were taken from the surface of TMM, while simulation shows the maximum temperature inside TMM.

4.4 Future Work

This study presents a noninvasive method for determining the spatial and thermal heating profiles in a phantom tissue heated by HIFU. This method can be used to confirm pre-clinical testing data submitted by device sponsors and verification of the basic transducer design and performance by Infrared measurement of generated heat or focusing characteristics. It can also be used to demonstrate that the device can produce predictable thermal dose. Optical properties of the tissue mimicking materials are less studied. These properties can be the topic of the future research in this field. Developing heat resistance, transparent and semi-transparent silicone based TMM, further investigation on optical properties of TMM, developing new simulation methods to consider the air layer effects, synchronizing excitation pulses with the camera frame rate to extract phase data (lock in phase thermography) and the HIFU beam forming by applying multiple harmonics at the same time (2.5 MHz and 7.5 MHz) can be considered for furthered investigation in this field.

APPENDIX A

TIMING AND GRID SIZE IN SIMUALTION

1) KZK numerical simulation grid and timing:

r direction element size: dr = 0.042 mm
Number of Elements: J = 753
Z Direction element size: dz = 0.037 mm
Number of elements: M = 2839

Timing progress for KZK equation:

z (cm)	time (hr:min:sec)
1.0	0:1:38.6
2.1	0:3:22.2
3.1	0:4:35.9
4.2	0:5:49.9
5.3	0:6:57.3
6.3	0:7:40.7
7.4	0:8:20.8
8.4	0:9:2.6
9.5	0:9:46.5
10.5	0:10:29.6

2) BHT numerical simulation grid and timing:

Time element size : dt = 0.06 sec
Number of time elements: N = 121
r Direction element size: dr = 0.08 mm
Number of elements: J = 151
Z Direction element size dz = 0.15 mm
Number of elements: M = 710

Timing progress for BHT equation:

t (sec)	time (hr:min:sec)
0.7	0:0:11.7
1.4	0:0:22.9
2.2	0:0:34.0
2.9	0:0:44.8
3.6	0:0:55.8
4.3	0:1:6.7
5.0	0:1:17.6
5.8	0:1:28.2
6.5	0:1:39.1
7.2	0:1:50.0

APPENDIX B

MATLAB CODES

```
%% Authored by Joshua Soneson 2007, updated 2012 by Mohammadreza
Jahangir Moghadam. This software is free to use.
function[u,U,Ppos,Pneg,I_td] = TDNL(u,U,X,K,J,c,cutoff,Ppos,Pneg,I_td)
% converts spectrum to one cycle of the timeUREdomain waveform and
% integrates the invicid Burger's equation using upwind/downwind
% method with periodic boundary conditions. TDNL stands for Time
% Domain NonLinear.

% set peak and trough values to zero; in case they are not assigned
later
if(K==1)    % linear case - do nothing
else        % nonlinear case - enter loop
  for j=J:-1:1
    % execute nonlinear step only if amplitude is above cutoff;
    % row j=1 is always computed so plots look nice and smooth!
    I_td(j) = 0;
    if(sqrt(u(j,1)*u(j,1) + u(J+j,1)*u(J+j,1))>cutoff | j==1)
      % convert from sin/cos representation to complex exponential
      U(2:K+1) = u(j,:) - i*u(j+J,:);
      U(2*K:-1:K+2) = u(j,1:K-1) + i*u(j+J,1:K-1);
      U(1) = 0;
      % transform to time domain:
      U = K*real(ifft(U));
      I_td(j) = trapz(U.^2);
      % determine how many steps necessary for CFL<1 (CFL<0.8 to be
safe).
      P = ceil(c*max(U)/0.8);
      % Nonlinear integration (upwind/downwind) algorithm
      for p=1:P
        for k=1:2*K
          if(U(k)<0)
            if(k==1)
              X(k) = U(k) + c*(U(1)*U(1) - U(2*K)*U(2*K))/P/2;
            else
              X(k) = U(k) + c*(U(k)*U(k) - U(k-1)*U(k-1))/P/2;
            end
          else
            if(k==2*K)
              X(k) = U(k) + c*(U(1)*U(1) - U(k)*U(k))/P/2;
            else
              X(k) = U(k) + c*(U(k+1)*U(k+1) - U(k)*U(k))/P/2;
            end
          end
        end
        U = X;
      end
      I_td(j) = I_td(j) - trapz(X.^2);
      % transform back to frequency domain:
      Ppos(j) = max(X);
      Pneg(j) = min(X);
      X = fft(X)/K;
      % convert back to sin/cos representation:
```

```
      u(j,:) = real(X(2:K+1));
      u(j+J,:) = -imag(X(2:K+1));
    end
  end
end
```

```
%% Authored by Joshua Soneson 2008, updated 2012 by Mohammadreza
Jahangir Moghadam. This software is free to use.

function[z,r,H,I,Ppos,Pneg]=axisymmetricKZK()
% Driver for axisymmetric KZK integrator.

% get system parameters:
[p0,c1,c2,rho1,rho2,N1,N2,G1,G2,gamma1,gamma2,a,b,d,f,R,Z,z_,K] =
KZK_parameters();
K2 = 2*K;

% print coefficients to screen:
fprintf('\n\tp0 = %2.2f MPa\n',1e-6*p0)
fprintf('\tN1 = %1.2f\tN2 = %1.2f\n',N1,N2)
fprintf('\tG1 = %3.2f\tG2 = %3.2f\n\n',G1,G2)

F=0.5*d/a;
if(F<1.37)
  fprintf('\tWarning--f/%1.2f exceeds the conditions\n',F)
  fprintf('\tunder which KZK is derived (> f/1.37).\n\n')
end

% grid set-up:
[M,J,J_,dz,dr,z,r]=computational_grid(Z,R,max(G1,G2),a,d,gamma2(1),N2)
;

% dependent variables:
u = zeros(2*J,K);
w = zeros(2*J,K);
limit = 1/sqrt(1-(a/d)^2);
v = initial_condition(J,K,G1,r,b*limit/a,limit);
v(1:J,1) = v(1:J,1).*sqrt(1-(r/d).^2);
v(J+1:2*J,1) = v(J+1:2*J,1).*sqrt(1-(r/d).^2);

% set up discretization operators:
for k=1:K
  [A1(k).IRK1,A1(k).IRK2,A1(k).CN1,A1(k).CN2] ...
  = KZK_operators(r,R,G1,dz,dr,J,k,gamma1(k));
  [A2(k).IRK1,A2(k).IRK2,A2(k).CN1,A2(k).CN2] ...
  = KZK_operators(r,R,G2,dz,dr,J,k,gamma2(k));
end
k1 = zeros(2*J,1);  % IRK slope vectors
```

```
k2 = zeros(2*J,1);
b1 = 1/sqrt(2);     % IRK coefficients
b2 = 1 - b1;

% parameters for nonlinear integration:
mu1 = N1*K*dz/pi;       % nonlinear term integration parameters
mu2 = N2*K*dz/pi;
cutoff1 = gamma1(1)/10/N1;  % cutoffs for performing nonlinear
integration
cutoff2 = gamma2(1)/10/N2;
X = zeros(1,K2);        % data vectors
Y = zeros(1,K2);
Xpeak = zeros(1,K2);

% for plotting routines:
H = zeros(J_,M);        % Heating rate matrix
H2 = zeros(J_,M);
H(:,1) = real(gamma1(1))*(v(1:J_,1).^2 + v(J+1:J+J_,1).^2);
I = zeros(J_,M);
I(:,1) = v(1:J_,1).^2 + v(J+1:J+J_,1).^2;
I_td = zeros(J,1);
dt = 1/f/(K2-1);
Ix = zeros(M,1);        % axial intensity vector
Ix(1) = v(1,1)^2 + v(J+1,1)^2;
Ir = zeros(J_,1);       % radial-focal intensity vector
if(K<5) kk = K; else kk = 5; end
p5x = zeros(kk,M);      % first (up to) 5 harmonic pressure amplitudes
p5x(1,1) = sqrt(v(1,1)*v(1,1) + v(J+1,1)*v(J+1,1));
p5r = zeros(kk,J_);
peak = zeros(M,1);      % waveform peak
trough = zeros(M,1);        % waveform trough
peak(1) = 1;
trough(1) = -1;

% for monitoring simulation:
amp_K = 0;          % amplitude of Kth harmonic

% for determining peak pressure waveform and location of its
occurence:
m_t = ceil(z_/dz/d);        % index of last meshpoint in material 1
if(m_t>M) m_t = M; end
m_f = round(M/Z);       % index of meshpoint nearest focus
p_peak = 0;         % peak axial pressure
z_peak = 0;         % distance at which peak axial pressure occurs
Ppos = zeros(J,M);
Pneg = zeros(J,M);

% integrate the equations through material 1:
fprintf('\tIntegrating KZK equation...\n')
fprintf('\t\tz (cm)\ttime (hr:min:sec)\n')
t_start = clock;
p1 = 0;
```

```
for m=1:m_t-1
  w = v;
  [v,X,Ppos(:,m),Pneg(:,m),I_td] = ...
    TDNL(v,X,Y,K,J,mu1,cutoff1,Ppos(:,m),Pneg(:,m),I_td);
  I_td = f*dt*I_td/dz;
  peak(m+1) = max(X);
  trough(m+1) = min(X);
  if(m==m_f)
    if(K>1)
      Ir = sum((v(1:J_,:)').^2);
      Ir = Ir + sum((v(J+1:J+J_,:)').^2);
    else
      Ir = v(1:J_).^2 + v(J+1:J+J_).^2;
    end
    p5r = sqrt(v(1:J_,1:kk).^2 + v(J+1:J+J_,1:kk).^2);
  end
  if(peak(m+1)>p_peak)
    p_peak = peak(m+1);
    z_peak = z(m+1);
    Xpeak = X;
  end
  if(z(m)<0.3)
    for k=1:K
      k1 = A1(k).IRK1 \ (A1(k).IRK2*v(:,k));
      k2 = A1(k).IRK1 \ (A1(k).IRK2*(v(:,k) + dz*b1*k1));
      u(:,k) = v(:,k) + dz*(b1*k1 + b2*k2);
    end
  else
    for k=1:K
      u(:,k) = A1(k).CN1 \ (A1(k).CN2*v(:,k));
    end
  end
  v = u;
  pl = sqrt(v(1,K).^2 + v(J+1,K).^2);
  if(pl > amp_K) amp_K = pl; end
  for j=1:J_
    H(j,m+1) = sum(real(gamma1(:)').*(u(j,:).^2 + u(J+j,:).^2));
    H2(j,m+1) = I_td(j);
    I(j,m+1) = sum(u(j,:).^2 + u(J+j,:).^2);
  end
  Ix(m+1) = sum(v(1,:).^2 + v(J+1,:).^2);
  if(Ix(m+1)>2*G1*G1)
    fprintf('\tStopped - computation became unstable at z = %2.1f
cm.\n',d*z(m))
    r = a*r(1:J_);
    z = d*z;
    KZK_radial_plots(r,Ir,H(:,round((M+1)/Z)),p5r,p0,rho2,c2,R,a);

KZK_axial_plots(z,Ix,p5x,H(1,:),peak,trough,p0,rho1,rho2,c1,c2,d,Z,a,m
_t)
    return
  end
  p5x(:,m+1) = sqrt(v(1,1:kk).*v(1,1:kk)+v(J+1,1:kk).*v(J+1,1:kk));
```

```
  p2 = floor(10*(m+1)/M);
  p1 = timing(p1,p2,t_start,z(m+1),d);
end

% material 2:
v = 2*rho2*c2*v/(rho1*c1+rho2*c2);
for m=m_t:M-1
  w = v;
  [v,X,Ppos(:,m),Pneg(:,m),I_td] = ...
    TDNL(v,X,Y,K,J,mu2,cutoff2,Ppos(:,m),Pneg(:,m),I_td);
  I_td = f*dt*I_td/dz;
  peak(m+1) = max(X);
  trough(m+1) = min(X);
  if(m==m_f)
    if(K>1)
      Ir = sum((v(1:J_,:)').^2);
      Ir = Ir + sum((v(J+1:J+J_,:)').^2);
    else
      Ir = v(1:J_).^2 + v(J+1:J+J_).^2;
    end
    p5r = sqrt(v(1:J_,1:kk).^2 + v(J+1:J+J_,1:kk).^2);
  end
  if(peak(m+1)>p_peak)
    p_peak = peak(m+1);
    z_peak = z(m+1);
    Xpeak = X;
  end
  if(z(m)<0.3)
    if(m==m_t)
      for k=1:K
        k1 = A1(k).IRK1 \ (A1(k).IRK2*v(:,k));
        k2 = A2(k).IRK1 \ (A2(k).IRK2*(v(:,k) + dz*b1*k1));
        u(:,k) = v(:,k) + dz*(b1*k1 + b2*k2);
      end
      u = (1-(rho1*c1-rho2*c2)/(rho1*c1+rho2*c2))*u;
    else
      for k=1:K
        k1 = A2(k).IRK1 \ (A2(k).IRK2*v(:,k));
        k2 = A2(k).IRK1 \ (A2(k).IRK2*(v(:,k) + dz*b1*k1));
        u(:,k) = v(:,k) + dz*(b1*k1 + b2*k2);
      end
    end
  else
    for k=1:K
      u(:,k) = A2(k).CN1 \ (A2(k).CN2*v(:,k));
    end
  end
  v = u;
  pl = sqrt(v(1,K).^2 + v(J+1,K).^2);
  if(pl > amp_K) amp_K = pl; end
  for j=1:J_
    H(j,m+1) = sum(real(gamma2(:)').*(u(j,:).^2 + u(J+j,:).^2));
    H2(j,m+1) = I_td(j);
```

```
    I(j,m+1) = sum(u(j,:).^2 + u(J+j,:).^2);
  end
  Ix(m+1) = sum(v(1,:).^2 + v(J+1,:).^2);
  if(Ix(m+1)>2*G2*G2)
    fprintf('\tStopped - computation became unstable at z = %2.1f
cm.\n',d*z(m))
    r = a*r(1:J_);
    z = d*z;
    KZK_radial_plots(r,Ir,H(:,round((M+1)/Z)),p5r,p0,rho2,c2,R,a);

KZK_axial_plots(z,Ix,p5x,H(1,:),peak,trough,p0,rho1,rho2,c1,c2,d,Z,a,m
_t);
    return
  end
  p5x(:,m+1) = sqrt(v(1,1:kk).*v(1,1:kk)+v(J+1,1:kk).*v(J+1,1:kk));
  p2 = floor(10*(m+1)/M);
  p1 = timing(p1,p2,t_start,z(m+1),d);
end
H(:,1:m_t) = 1e-4*p0*p0*H(:,1:m_t)/rho1/c1/d;   % dimensionalize H
H(:,m_t+1:M) = 1e-4*p0*p0*H(:,m_t+1:M)/rho2/c2/d;
H2(:,1:m_t) = 1e-4*0.5*p0*p0*H2(:,1:m_t)/rho1/c1/d; % dimensionalize H
H2(:,m_t+1:M) = 1e-4*0.5*p0*p0*H2(:,m_t+1:M)/rho2/c2/d;
H = real(H + H2);
I(:,1:m_t) = 1e-4*0.5*p0*p0*I(:,1:m_t)/rho1/c1; % dimensionalize I
I(:,m_t+1:M) = 1e-4*0.5*p0*p0*I(:,m_t+1:M)/rho2/c2;


fprintf('\tmax(|p_K|/p0) = %e\n',amp_K)

r = a*r(1:J_);  % rescale r and chop so that PML region is excluded in
plots
z = d*z;    % rescale z
Ppos = Ppos(1:J_,:);
Pneg = Pneg(1:J_,:);

% call plotting routines:
if(K>1)
  plot_waveform(p0,f,Xpeak,d*z_peak,K2);
end
KZK_radial_plots(r,Ir,H(:,round((M+1)/Z)),p5r,p0,rho2,c2,R,a);
KZK_axial_plots(z,Ix,p5x,H(1,:),peak,trough,p0,rho1,rho2,c1,c2,d,Z,a,m
_t);
```

```
%% Authored by Joshua Soneson 2008, updated 2012 by Mohammadreza
Jahangir Moghadam. This software is free to use.
function[Tmax_mat,Dmat] = axisymmetricBHT(z,r,H)
% Bioheat transfer equation integrator

% get parameters:
[p0,c1,c2,rho1,rho2,N1,N2,G1,G2,gamma1,gamma2,a,b,d,f,R,Z,z_,K] = ...
KZK_parameters();

% get more parameters:
[C1,C2,k1,k2,w1,w2,N,t,input,dt,J,M,z,r,H,T0] = BHT_parameters(z,r,H);
D1 = 1e4*k1/C1/rho1;            % diffusivity of material 1
D2 = 1e4*k2/C2/rho2;            % diffusivity of material 2
P1 = w1/rho1;
P2 = w2/rho2;

% create Crank-Nicolson operators for BHT:
[A,B] = BHT_operators(r,z,D1,D2,P1,P2,dt,z_/d/Z);
m_ = round(z_*M/d/Z);           % index @ material interface
if(m_>M) m_ = M; end
H(:,1:m_) = 1e6*H(:,1:m_)/C1/rho1;  % rescale H to degrees/second
H(:,m_+1:M) = 1e6*H(:,m_+1:M)/C2/rho2;

JM = J*M;
Q = zeros(JM,1);            % heating source vector
T = zeros(JM,1);            % temperature vector
D = zeros(JM,1);            % thermal dose vector
Tmat = zeros(J,M);          % temp matrix
Dmat = zeros(J,M);          % dose matrix
Q = vektorize(Q,H,J,M);         % column-stack the heat matrix
s1 = zeros(JM,1);           % slopes for IRK integrator
s2 = zeros(JM,1);
Tpeak = zeros(N,1);         % temp vs time vector
Tmax_vec = zeros(JM,1);         % max temp distribution vector
Tmax_mat = zeros(J,M);          % max temp distribution matrix
tt = 0;

% Integrate BHT:
fprintf('\tIntegrating BHT equation...\n')
fprintf('\t\tt (sec)\ttime (hr:min:sec)\n')
t_start = clock;
p1 = 0;
for n=1:N-1
  s1 = A*T + input(n)*Q;
  s2 = B \ (A*(T+0.5*dt*s1) + input(n+1)*Q);
  T = T + 0.5*dt*(s1+s2);
  D = D + equivalent_time(T,JM,T0);
  Tpeak(n+1) = max(T);
  if(Tpeak(n+1)>tt)
    tt = Tpeak(n+1);
    Tmax_vec = T;
```

```
    t_peak = t(n+1);
  end
  p2 = floor(10*(n+1)/N);
  p1 = timing(p1,p2,t_start,t(n+1),1);
end

Tmax_mat = matrixize(Tmax_vec,Tmax_mat,J,M);
Dmat = dt*matrixize(D,Dmat,J,M)/60;
BHT_plots(z,r,t,t_peak,Tpeak,Tmax_mat,Dmat,T0)
```

REFERENCES

[1] R. A. Novelline and L. F. Squire, Squire’s fundamentals of radiology. Cambridge, Mass. Harvard University Press, 2004.

[2] N. McDannold, S. Fossheim,H. Rasmussen, H. Martin, N. VykhodtsevaandK. Hynynen, Heat-activated liposomal MRcontrast agent: initial in vivo results in rabbit liver and kidney,”Radiology,230:743-752, 2004.

[3] F. Wu, Z. Wang, W. Chen, J. Bai, H. ZhuandT. Qiao, “Preliminary experience using high intensity focused ultrasound for the treatment of patients with advanced stage renal malignancy,” J. Urol., 170:2237-2240, 2003.

[4] J. Tavakkoli, V. V. Rao, R. Seip, R. F. Paterson, E. Barret, L. Cheng, A.L.Shalhavand N.T.Sanghvi, “Laparoscopic high intensity focused ultrasound: application to kidney ablation,” Int.Symp.Ther.Ultrasound, Seattle, USA, 2002.

[5] J. E. Kennedy, F. Wu, G.R.ter Haar, F.V.Gleeson, R.R.Phillips, M. R. MiddletonandD. Cranston, “High-intensity focused ultrasound for the treatment of liver tumors,” Ultrasonics, 42:931-935, 2004.

[6] W. Hundt, E. Yuh, M. BednarskiandS. Guccione, “Gene expression profiles, histologic analysis, and imaging of squamous cell carcinoma model treated with focused ultrasound beams,”Am.J.Roentgenol., 189:726-736, 2007.

[7] H. Beerlage, S. Thuroff, F. Debruyne, C. ChaussyandJ. de la Rosette, “Transrectal high-intensity focused ultrasound using the Ablatherm device in the treatment of localized prostate carcinoma,” Urology, 54:273-277, 1999.

[8] P. Huber, J. Jenne, R. Rastert, I. Simiantonakis, H. Sinn,H. Strittmatter, D. Fournier, M. WannenmacherandJ. Debus, “A new noninvasive approach in breast cancer therapy using

magnetic resonance imaging-guided focused ultrasound surgery," Cancer Res., 61:8441-8447, 2001.

[9] http://clinicaltrial.gov/ct2/show/NCT00772317?term=hifu&rank=8

[10] Schafer, Mark E., James Gessert, and Wayne Moore. "Development Of A High Intensity Focused Ultrasound (HIFU) Hydrophone System." AIP Conference Proceedings 829.1 (2006): 609-613. Academic Search Complete. Web. 11 Feb. 2012.

[11] P. A. Lewin and M. E. Schafer, "Shock wave sensors: I. Requirements and design," J. Lithotripsy Stone Disease, vol. 3, pp. 3–17, 1991.

[12] C. C. Coussios , C. H. Farny , C. R. Thomas , R. O. Cleveland , R. G. Holt and R. A. Roy "Cavitation detection during and following HIFU exposure in vitro", J. Acoust. Soc. Amer., vol. 115, p.2448 , 2004.

[13] K. R. Gorny , N. J. Hangiandreou , G. K. Hesley , B. S. Gostout , K. P. McGee and J. P. Felmlee "MR guided focused ultrasound: Technical acceptance measures for a clinical system", Phys. Med. Biol., vol. 51, p.3155 , 2006.

[14] Stride, E P, C C Coussios, and Peter N T Wells. "Cavitation and Contrast: The Use of Bubbles in Ultrasound Imaging and Therapy." Proceedings of the Institution of Mechanical Engineers, Part H: Journal of Engineering in Medicine 224.2 (2010): 171-191. Web. 11 Feb. 2012.

[15] Oleg A. Sapozhnikov, et al. "Acoustic Characterization Of High Intensity Focused Ultrasound Fields: A Combined Measurement And Modeling Approach." Journal Of The Acoustical Society Of America 124.4 (2008): 2406-2420. Academic Search Complete. Web. 13 Feb. 2012.

[16] Harris, G.R.; , "FDA regulation of clinical high intensity focused ultrasound (HIFU) devices," Engineering in Medicine and Biology Society, 2009. EMBC 2009. Annual International Conference of the IEEE , vol., no., pp.145-148, 3-6 Sept. 2009
doi: 10.1109/IEMBS.2009.5332444

[17] G. Harris, "Medical ultrasound exposure measurements: Update on devices, methods, and problems," Proc.-IEEE Ultrason. Symp. 2, 1341–1352 (1999).

[18] E. Filonenko and V. Khokhlova, “Effect of acoustic nonlinearity on heating of biological tissue by high-intensity focused ultrasound,” Acoust. Phys. **47**, 541–549 (2001).

[19] Y. Zhou, L. Zhai, R. Simmons, and P. Zhong, “Measurement of high intensity focused ultrasound fields by a fiber optic probe hydrophone,” J. Acoust. Soc. Am. **120**, 676–685 (2006)

[20] J. Parsons, C. Cain, and J. Fowlkes, “Cost-effective assembly of a basic fiber-optic hydrophone for measurement of high-amplitude therapeutic ultrasound fields,” J. Acoust. Soc. Am. **119**, 1432–1440 (2006).

[21] M. Averkiou and R. Cleveland, “Modeling of an electrohydraulic lithotripter with the KZK equation,” J. Acoust. Soc. Am. 106, 102–112 (1999)

[22] Wensheng Shen, Jun Zhang, Fuqian Yang, Modeling and numerical simulation of bioheat transfer and biomechanics in soft tissue, Mathematical and Computer Modelling, Volume 41, Issues 11–12, May 2005, Pages 1251-

[23] M. A. Averkiou and M. F. Hamilton, “Nonlinear distortion of short pulses radiated by plane and focused circular pistons,” Journal of the Acoustical Society of America, vol. 102, no. 5, pp. 2539–2548, 1997.

[24] Pinton, Gianmarco F. and Trahey, Gregg E., Numerical methods for axisymmetric and 3D nonlinear beams, Proceedings - IEEE Ultrasonics Symposium, vol 2 (2005), pp. 1291 – 1294.

[25] Y.-S. Lee and M. F. Hamilton, “Time-domain modeling of pulsed finiteamplitude sound beams,” Journal of the Acoustical Society of America, vol. 97, no. 2, pp. 906–917, February 1995

[26] M. F. Hamilton and D. T. Blackstock. Nonlinear Acoustics. Academic Press, San Diego, 1997.

[27] Yang-Sub Lee and Mark F. Hamilton. Time-domain modeling of pulsed finite amplitude sound beams. J. Acoust. Soc. Am., 97(2):906–917, February 1995.

[28] S. K. Godunov. A finite difference method for the numerical computation and discontinuous solutions of the equations of fluid dynamics. Mat. Sb., 47:271– 306, 1959.

[29] M. F. Hamilton, V. A. Khokhlova, and O. V. Rudenko, “Analytical method for describing the paraxial region of finite amplitude sound beams,” Journal of the Acoustical Society of America, vol. 101, no. 3, pp. 1298–1308, March 1997.

[30] Maggi, L.E.; von Kruger, M.A.; Pereira, W.C.A.; Monteiro, E.; , "Development of silicon-based materials for ultrasound biological phantoms," Ultrasonics Symposium (IUS), 2009 IEEE International , vol., no., pp.1962-1965, 20-23 Sept. 2009

[31] Acoustical properties of selected tissue phantom materials for ultrasound imaging Source: Physics in medicine and biology [0031-9155] Zell, K yr:2007 vol:52 iss:20 pg:N475

[32] J.W. Durkee Jr. and P.P. Antich, Exact solutions to the multi-region time-dependent bioheat equation with transient heat sources and boundary conditions, Phys. Med. Biol. 36, 345-368, (1991).

BIOGRAPHICAL INFORMATION

Mohammadreza Jahangir Moghadam was born in Tehran, Iran, on May 1977. After graduation from Isfahan University of Technology in 2001 he entered the Electrical and Computer Engineering Research Center (ECERC) in 2002 and was a cofounder of Plasmatavan Company at Isfahan Science and Technology Town (ISCT) in 2007. He entered the Master of Science degree at University of Arlington in Texas in 2009. He has worked several semesters as a teaching and research assistant for medical imaging and digital electronic courses. He is also a student member of IEEE and member of HKN honor society of electrical engineers. He received UTA president award for best presentation on sustainability at Annual Celebration of Excellence by Students (ACES) in 2011. He is nominated for 2012 department of electrical engineering outstanding GTA award.